A high order discontinuous Galerkin method for the symmetric form of the anisotropic viscoelastic wave equation

Khemraj Shukla*, Jesse Chan, Maarten V. de Hoop

Department of Computational and Applied Mathematics, Rice University, 6100 Main St, Houston, TX, 77005

Abstract

We introduce a new symmetric treatment of anisotropic viscous terms in the viscoelastic wave equation. An appropriate memory variable treatment of stress-strain convolution terms, result into a symmetric system of first order linear hyperbolic partial differential equations, which we discretize using a high-order discontinuous Galerkin finite element method. The accuracy of the resulting numerical scheme is verified using convergence studies against analytical plane wave solutions and analytical solutions of the viscoelastic wave equation. Computational experiments are shown for various combinations of homogeneous and heterogeneous viscoelastic media in two and three dimensions.

1. Introduction

Numerical solution of elastic wave equation are essential for various imaging problems arising at different scales. At global scale, elastic waves travels through the entire Earth and allow geophysicists to infer properties and structure of the Earth interior. At a macro-scale, elastic waves can be used to image and characterize oil and gas reservoirs. On a micro or laboratory scale, elastic waves play a major role in studying the micro-structure of materials. To solve the elastic wave equation accurately, the input model should be able to accommodate arbitrary variations of petrophysical and lithological properties, as they play an important role, particularly in the targets of exploration geophysics, i.e., reservoir rocks. To study reservoir monitoring and evaluation of rock properties in a laboratory setting, lithological and reservoir properties become more important. Reservoir rocks such as cracked limestones can show effective anisotropy in the low frequency band. On the other hand, fluid-filled cracked and porous rocks show considerable attenuation properties, which is not incorporated in vanilla elastic approximation. Experimental work also shows that anisotropy effects of attenuation are more pronounced than anisotropic elastic effects [1, 2]. Therefore, a realistic rheology is required to model anisotropic attenuation characteristics.

Various dissipation mechanisms (e.g. Kelvin-Voigt, Maxwell, Zener or Simple Linear Solid) [3], expressed by a time dependent relaxation function, can be modeled by a viscoelastic constitutive relation. Attenuation of energy is caused by a large variety of dissipation mechanisms and incorporating all these mechanism into a general microstructure is very difficult [4]. For example, modeling of dissipation in isotopic media is very simple and will require only two relaxation functions, one for each decoupled wave modes (dilatational and shear modes). Therefore, only two relaxation functions are enough to describe anelastic characteristics of body waves. However, in anisotropic media one has to consider 21 frequency (time) dependent stiffness parameters to address dissipation mechanism accurately. Subsequently, Mehrabadi and Cowin [5] and Helbig [6] presented that only six of the 21 stiffness parameters have an intrinsic physical meaning. Motivated by the studies of of Mehrabadi and Cowin [5] and Helbig [6], Carcione formulated a constitutive model and wave equations for linear viscoelastic anisotropic media [7]. In a three-dimensional anisotropic media,

*corresponding author

Email addresses: rajexplo@gmail.com (Khemraj Shukla), jesse.chan@rice.edu (Jesse Chan), mdehoop@rice.edu (Maarten V. de Hoop)

careful attention is required while modeling the properties of the shear modes, as relaxations of the medium can be different for slow and fast shear modes. Therefore, Carcione [3] used single relaxation function to model the anelastic properties of the quasi-dilatational mode, whereas he uses three relaxation functions to control the dissipation of the medium due to shear waves. In this paper, we use the constitutive model proposed by Caricone [8], paired it with equations of motion described by Newton's second law of motion and thereafter symmetrized the system by performing change of variables operation on memory variables induced by dissipation process. This entire exercise results into a system of first order hyperbolic partial differential equations (PDEs) with stress, velocity and memory variables (only time dependent) as field variables.

The elastic wave equation is a system of first order hyperbolic partial differential equations, which can be solved using any suitable numerical method such as finite-differences, finite volumes and finite element methods. A detailed overview of these methods is given by [9, 10]. The most popular and simple method is the finite-difference (FD) method, and its application to the elastic wave equation has been studied by many researchers [11, 12, 13, 14, 15]. A detailed numerical analysis of finite-difference methods is given in [16]. Although the numerical representation of FD method is very simple, but often comes with significant numerical dispersion, especially in the modeling of surface waves [12]. Additionally, the implementation of boundary conditions can require special treatment [17]. FD methods are also difficult to apply to irregular geometries with out experiencing "staircase effects" [17]. To circumvent the effect of numerical dispersion and achieve high order accuracy, pseudo-spectral methods were first used by Tessmer and Kosloff [18]. The pseudo-spectral method uses global basis function for approximation of the solutions (e.g., Fourier or Chebyshev). The pseudo-spectral method requires few grid points per wavelength and produces a high order solution with less numerical dispersion. However, the choice of the global basis functions restricts the pseudo-spectral methods to smooth models, as it is difficult to represent materials with the discontinuities or sharp contrast. This can be addressed somewhat using domain decomposition, where different meshes are used to represent the different domains. For example, Carcione [19] used Fourier basis functions along directions with smoothly varying materials properties and Chebyshev basis functions in directions with sharply varying medium properties.

The finite element method (FEM) discretizes the domain using elements e.g., triangles and quadrilaterals in 2D and tetrahedral and hexahedrals in 3D and solves the spatial derivatives of PDEs. The wave propagation in time-domain is expressed by a hyperbolic system of partial differential equations and rarely results into a stiff system. Therefore, an explicit time integration scheme e.g. Runge-Kutta or Euler schemes, could be efficiently applied as the requirement of CFL condition for time stability are easily satisfied. However, pairing of finite-element methods (used for spatial discretization) with an explicit time-integration scheme requires inversion of a global mass matrix, which causes a computational bottleneck especially for the large computational domain. However, various methods are proposed to avoid the inversion of global mass matrix. In particular, the approach of diagonal mass lumping [20], which transforms the global mass matrix into a diagonal matrix by summing all line coefficients of matrix onto the diagonal elements [21]. Finite element method for elastic wave equation are studied by Marfurt [12] and Bao *et al.* [22]. In these works, FEM was shown to accurately represent sharp material properties and irregular geometries. However, the solution on each element is approximated using a low order polynomials, which results in significant numerical dispersion. In order to recover a more accurate solution high order elements are required which results into large matrices to be inverted at each time step of time integration. To exploit the spectral properties in the finite element method, Patera [23] proposed the spectral element method (SEM) to solve fluid flow problems. Subsequently, the SEM was successfully implemented by Seriani *et al.* [24] to solve the acoustic wave equation in a heterogeneous medium. Komatitsch and Vilotte [25] used SEM to solve the elastic wave equation in a heterogeneous medium, described by a system of the second order PDEs. A detailed review of methods adopted in wave field modeling is presented by Carcione *et al.* [26].

In this paper, a high-order numerical scheme based on the nodal discontinuous Galerkin method is introduced to solve the symmetrized 3D viscoelastic wave equation. The descretization of the domain is performed by using unstructured tetrahedron (hexahedra) and and triangular (quadrilateral) meshes in 3D and 2D, respectively. The implementation of high order methods provide (1) high accuracy in numerical solution, and (2) flexibility in accommodating unstructured meshes, which are required for discretization of

complex geometries. The efficacy of discontinuous Galerkin (DG) method in solving linear and non-linear time-dependent hyperbolic problems is shown by Hesthaven *et al.* [27]. Additionally, A natural adoption of DG method on a heterogeneous computing environment (CPU + GPUs) makes them more advantageous in terms of computational cost while solving time dependent hyperbolic problems [28]. In comparison to low order methods the DG method offers low numerical dissipation and dispersion [29] resulting into solutions with high accuracy. The effect of dispersion and dissipation in numerical solutions becomes more troublesome when long time integration is required, e.g. simulation of elastic wave over the Earth or Tsunami simulation. However, Wilcox *et al.* [30] has shown that DG method made it possible to solve the elastic wave equation over a long time domain with a very high order accuracy. The weak formulation for second order elastic wave equation proposed by Komatitsch [25] uses discretely orthogonal nodal basis functions along with under-integrated L^2 inner product. This approach produces diagonal mass matrices for quadrilateral and hexahedral elements. However, in the high order DG methods, locally invertible block diagonal mass matrices are induced and the inverse of these block diagonal matrices could be computed computed concurrently. The size of these block diagonal matrices are $N_p \times N_p$, with N_p being degree of freedoms over an element. Many researchers have successfully implemented high order DG methods with simplicial meshes for solution of elastic and acoustic waves exist in literature [31, 32, 33].

In DG methods, first the solution is approximated locally over the elements. Thereafter, a global approximation of solution is recovered by imposing (weakly) the continuity of local solutions at opposite faces (edges in 2D) of the elements through a numerical flux. In particular, the upwind flux (solution of a Riemann problems) is more frequently employed [34] to recover the global solution. Käser *et al.* [31] solved the 3D isotropic viscoelastic wave equation in a strain-velocity formulation using a local space-time DG method with an upwind flux by solving the exact Riemann problem on inter-element boundaries. In another study, Lambrecht *et al.* [35] used a nodal DG method to solve the isotropic viscoelasltic wave equation using the same formulation proposed by Käser et al. [31]. The choice of numerical flux also results into providing the stability to numerical scheme and controlling the numerical dissipation. Therefore, choosing the solution of the Riemann problem as a numerical flux becomes obvious as these are less dissipative than any standard numerical flux. However, the first step for solving the Riemann problem is diagonalization of Jacobian matrices into polarized wave modes [36], resulting into a computationally intensive process especially for the systems with unstructured Jacobian matrices. Additionally, solution of Riemann problem for isotropic system does not extend naturally to anisotropic materials and therefore requires the re-computation of Riemann solvers. The various studies have been carried out on avoiding the diagonalization of Jacobian matrices using penalty fluxes based on natural boundary conditions [33, 37, 38, 39]. The penalty fluxes are easy to implement and provide accuracy and dissipation similar to fluxes based on solution of Riemann problems. In this study, we implemented similar energy-stable penalty flux for the anisotropic viscoelastic wave equations.

The main new contributions of this paper are a new symmetric form of the anisotropic viscoelastic wave equation and its discretization using a high order DG method using penalty fluxes. The outline of the paper is as follows: Section 2 will briefly review the system of equations describing the viscoelastic wave equation. Section 4 presents an energy stable formulation for the symmetric hyperbolic form of the viscoelastic wave equations. Finally, numerical results in Section 5 demonstrate the accuracy of this method for several 2D and 3D problems arising in linear anisotropic viscoelasticity.

2. Constitutive Relations

In this section, subsections (2.1)-(2.4) briefly review the formulations of non-symmteric form of the system of viscoelastic wave equation obtained by Carcione [8, 7].

2.1. Convolution and Boltzmann relation

The Riemann convolution between time dependent functions f with g is defined as

$$f * g = \begin{cases} \int_0^t f(\tau) g(t-\tau)\, d\tau : & t \geqslant 0 \\ 0 : & t < 0, \end{cases} \tag{1}$$

where t is the time variable.

The Boltzman operation [40] defines the time derivative of the convolution between Heaviside type function, f and g as

$$f * \partial_t g = f \odot g = \mathring{f} g + \left(\dot{f} H\right) * g, \tag{2}$$

where $\mathring{f} = f(t = 0^+)$ and $H(t)$ is the step function.

2.2. Stress-strain relations

The general constitutive relation for an anisotropic and linear viscoelastic medium can be expressed as [8]

$$\boldsymbol{\sigma} = \dot{\boldsymbol{\Psi}} * \boldsymbol{\epsilon} \tag{3}$$

where $\boldsymbol{\sigma} = [\sigma_{11}, \sigma_{22}, \sigma_{22}, \sigma_{23}, \sigma_{13}, \sigma_{12}]^T$, $\boldsymbol{\epsilon} = [\epsilon_{11}, \epsilon_{22}, \epsilon_{33}, \epsilon_{23}, \epsilon_{13}, \epsilon_{12}]^T$ are stress and strain vectors with $\gamma_{ij} = 2\epsilon_{ij}$, sub-indices 1 to 3 correspond to the three Cartesian coordinates x, y and z, and $\boldsymbol{\Psi}$ is the symmetric relaxation matrix, expressed as [7]

$$\boldsymbol{\Psi} = \begin{bmatrix} \psi_{11} & \psi_{12} & \psi_{13} & c_{14} & c_{15} & c_{16} \\ & \psi_{22} & \psi_{23} & c_{24} & c_{25} & c_{26} \\ & & \psi_{33} & c_{34} & c_{35} & c_{36} \\ & & & c_{44}\chi_2 & c_{45} & c_{46} \\ & & & & c_{55}\chi_3 & c_{56} \\ & & & & & c_{66}\chi_4 \end{bmatrix} H(t),$$

with

$$\psi_{i(I)} = c_{I(I)} - D + K\chi_1 + \frac{4}{3} G\chi_\delta \qquad \text{for } I = 1, 2, 3$$
$$\psi_{IJ} = c_{IJ} - D + 2G + K\chi_1 - \frac{2}{3} G\chi_\delta \qquad \text{for } I, J = 1, 2, 3; I \neq J.$$

The c_{IJ} for $I, J = 1, ..., 6$ are the high-frequency limit (unrelaxed) elasticities i.e. $t \to 0; \omega \to \infty$, and

$$K = D - \frac{4}{3} G,$$

where

$$D = \frac{1}{3}(c_{11} + c_{22} + c_{33}), \qquad G = \frac{1}{3}(c_{44} + c_{55} + c_{66}).$$

The χ_ν are dimensionless relaxation function with index $\nu = 1$ representing the quasi-dilatational mode and indices $\nu = 2, 3, 4$ corresponds to shear waves. χ_δ is a shear relaxation function for $\delta = 2, 3$, or 4. $H(t)$ is the Heaviside function.

In this study, the following relaxation functions are used [3]

$$\chi_\nu(t) = L_\nu \left(\sum_{l=1}^{L_\nu} \frac{\tau_{\epsilon l}^{(\nu)}}{\tau_{\sigma l}^{(\nu)}} \right) \left[1 - \frac{1}{L_\nu} \sum_{l=1}^{L_\nu} \left(1 - \frac{\tau_{\epsilon l}^{(\nu)}}{\tau_{\sigma l}^{(\nu)}} \right) \exp\left(-t/\tau_{\sigma l}^{(\nu)} \right) \right], \qquad \nu = 1, ..., 4, \tag{4}$$

where $\tau_{\epsilon l}^{(\nu)}$ and $\tau_{\sigma l}^{(\nu)}$ are material relaxation times such that $\tau_{\epsilon l}^{(\nu)} \geqslant \tau_{\sigma l}^{(\nu)}$. The pair $\tau_{\epsilon l}^{(\nu)}$ and $\tau_{\sigma l}^{(\nu)}$ define a dissipation mechanism.

Equation (4) describes the relaxation function of generalized standard linear solid (also known as Zener model) consisting of L_ν elements [1] connected in parallel. The complex modulus of the system is [3]

$$M_\nu(\omega) = \mathcal{F}\left(\frac{d[\chi_\nu(t)H(t)]}{dt}\right), \tag{5}$$

where ω is the angular frequency and $\mathcal{F}(\cdot)$ represents the time Fourier transform of the variable.

$M_\nu(\omega)$ is expressed as

$$M_\nu(\omega) = L_\nu \sum_{l=1}^{L_\nu} \frac{1 + i\omega\tau_{\epsilon l}^{(\nu)}}{1 + i\omega\tau_{\sigma l}^{(\nu)}}. \tag{6}$$

From (6) it can be easily seen that $M_\nu(0) = 1$ as $\dfrac{\tau_{\epsilon l}^{(\nu)}}{\tau_{\sigma l}^{(\nu)}} \to 1$, which gives the low frequency limit. Thus, (6) is a general relaxation function which can recover all possible type of frequency behavior of attenuation and velocity dispersion observed in subsurface materials.

2.3. Strain memory variables

The stress–strain relation in time domain is expressed as

$$\sigma_I = \psi_{IJ} * \partial_t e_J \tag{7}$$

Application of the Boltzmann operation (2) to (7) yields

$$\sigma_I = \mathring{\psi}_{IJ} e_J + \left(\dot{\psi}_{IJ} H\right) * e_J \tag{8}$$

Now we use

$$\breve{\phi}_{\nu l}(t) = \dot{\chi}_\nu(t) = \frac{1}{\tau_{\sigma l}^{(\nu)}} \left(\sum_{l=1}^{L_\nu} \frac{\tau_{\epsilon l}^{(\nu)}}{\tau_{\sigma l}^{(\nu)}}\right) \left(1 - \frac{\tau_{\epsilon l}^{(\nu)}}{\tau_{\sigma l}^{(\nu)}}\right) \exp\left(-t/\tau_{\sigma l}^{(\nu)}\right)$$

and write (8) in matrix form, which is expressed as

$$\sigma_I = A_{IJ}^{(\nu)} e_J + B_{IJ}^{(\nu)} \sum_{l=1}^{L_\nu} e_{Jl}^{(\nu)}, \tag{9}$$

where A's and B's are the matrices formed by the combination of elastic constants c_{IJ} and

$$e_{Jl}^{(v)} = \phi_{\nu l}(t) * e_J, \qquad J = 1, .., 6, \qquad l = 1, .., L_\nu, \quad \nu = 1, .., 4,$$

where $\phi_{\nu l} = \breve{\phi}_{\nu l}(t)H(t)$ are the components of 6×1 strain memory array $\boldsymbol{e}_l^{(\nu)}$.

In 3D, the symmetric strain memory tensor corresponding to the l^{th} dissipation mechanism of the relaxation function χ_ν is expressed as [7]

$$\boldsymbol{e}_{\boldsymbol{l}}^{(\boldsymbol{\nu})} = \begin{bmatrix} e_{11l}^{(\nu)} & e_{12l}^{(\nu)} & e_{13l}^{(\nu)} \\ & e_{22l}^{(\nu)} & e_{23l}^{(\nu)} \\ & & e_{33l}^{(\nu)} \end{bmatrix} = \phi_{\nu l} * \begin{bmatrix} \epsilon_{11} & \gamma_{12} & \gamma_{13} \\ & \epsilon_{22} & \gamma_{23} \\ & & \epsilon_{33} \end{bmatrix} \tag{10}$$

$$= \phi_{\nu l}(t) * e_J. \tag{11}$$

[1] A mechanical system in which a spring and a parallel combination of a dashpot and a spring are connected in series.

The tensor $\boldsymbol{e}_{\boldsymbol{l}}^{(\boldsymbol{\nu})}$ contains the past history of material due the dissipation mechanism defined in (4). In the pure elastic case $\tau_{\epsilon l}^{(\nu)} \to \tau_{\sigma l}^{(\nu)}$, $\phi_{\nu l} \to 0$ and $\boldsymbol{e}_{\boldsymbol{l}}^{(\boldsymbol{\nu})}$ vanishes.

Similar to the strain tensor, the memory strain variable can be decomposed as

$$\boldsymbol{e}_{\boldsymbol{l}}^{(\nu)} = \boldsymbol{d}_l^{(\nu)} + \left(\frac{1}{3}\mathrm{tr}(\boldsymbol{e}_l^{(\nu)})\right)\boldsymbol{I}, \qquad \mathrm{tr}\left(\boldsymbol{d}_l^{(\nu)}\right) = 0, \tag{12}$$

where $\boldsymbol{d}_l^{(\nu)}$ is the deviatoric strain memory tensor which is traceless and $\boldsymbol{I}$ is 3×3 identity matrix. Thus, the dilatation and shear memory variables are defined as

$$e_{1l} = \mathrm{tr}\left(\boldsymbol{e}_l^{(1)}\right), \qquad \text{and} \qquad e_{ijl} = \left(\boldsymbol{d}_l^{(\nu)}\right)_{ij}, \tag{13}$$

where $\nu = \delta$ for $i = j$, $\nu = 2$ for $ij = 23$, $\nu = 3$ for $ij = 13$ and $\nu = 4$ for $ij = 12$.

The stress-strain relations in terms of strain components and memory variables with one dissipation mechanism for each mode are [7]

$$\sigma_{11} = c_{11}\epsilon_{11} + c_{12}\epsilon_{22} + c_{13}\epsilon_{33} + c_{14}\gamma_{23} + c_{15}\gamma_{13} + c_{16}\gamma_{13} + Ke_{11} + 2Ge_{111}^{(\delta)} \tag{14a}$$

$$\sigma_{22} = c_{12}\epsilon_{11} + c_{22}\epsilon_{22} + c_{23}\epsilon_{33} + c_{24}\gamma_{23} + c_{25}\gamma_{13} + c_{26}\gamma_{12} + Ke_{11} + 2Ge_{221}^{(\delta)} \tag{14b}$$

$$\sigma_{33} = c_{13}\epsilon_{11} + c_{23}\epsilon_{22} + c_{33}\epsilon_{33} + c_{34}\gamma_{23} + c_{35}\gamma_{13} + c_{36}\gamma_{12} + Ke_{11} - 2G\left(e_{111}^{(\delta)} + e_{221}^{(\delta)}\right) \tag{14c}$$

$$\sigma_{23} = c_{14}\epsilon_{11} + c_{24}\epsilon_{22} + c_{34}\epsilon_{33} + c_{44}\gamma_{23} + c_{44}e_{231}^{(2)} + c_{45}\gamma_{13} + c_{46}\gamma_{13} \tag{14d}$$

$$\sigma_{13} = c_{15}\epsilon_{11} + c_{25}\epsilon_{22} + c_{35}\epsilon_{33} + c_{45}\gamma_{23} + c_{55}\gamma_{23} + c_{55}e_{131}^{(3)} + c_{56}\gamma_{12} \tag{14e}$$

$$\sigma_{12} = c_{16}\epsilon_{11} + c_{26}\epsilon_{22} + c_{36}\epsilon_{33} + c_{46}\gamma_{23} + c_{56}\gamma_{13} + c_{66}\gamma_{13} + c_{66}e_{121}^{(4)} \tag{14f}$$

$$\tag{14g}$$

where $c_{IJ} = \psi_{IJ}(t = 0^+)$ are unrelaxed elasticity constant at $\omega \to \infty$.

2.4. Memory variable equation

Application of the Boltzman equation to the deviatoric part of (11) yields

$$\partial_t \boldsymbol{d}_l^{(\nu)} = \phi_{\nu l}(0)\boldsymbol{d} + (\partial_t \breve{\phi}_{\nu l} H) * \boldsymbol{d}. \tag{15}$$

Here, $\boldsymbol{d}$ denotes the deviatoric strain tensor with elements

$$\boldsymbol{d} = \boldsymbol{\epsilon} - \frac{1}{3}\mathcal{V}\boldsymbol{I}, \tag{16}$$

where the strain tensor $\boldsymbol{\epsilon}$ and $\mathcal{V}$ are

$$\boldsymbol{\epsilon} = \begin{bmatrix} \epsilon_{11} & \epsilon_{12} & \epsilon_{13} \\ \epsilon_{12} & \epsilon_{22} & \epsilon_{23} \\ \epsilon_{13} & \epsilon_{23} & \epsilon_{33} \end{bmatrix}, \qquad \mathcal{V} = \epsilon_{11} + \epsilon_{22} + \epsilon_{33}.$$

Using $\partial_t \breve{\phi}_{\nu l} = -\dfrac{\breve{\phi}_{\nu l}}{\tau_{\sigma l}^{(\nu)}}$ and substituting it in (15), we recover

$$\partial_t \boldsymbol{d}_l^{(\nu)} = \phi_{\nu l}(0)\boldsymbol{d} - \frac{1}{\tau_{\sigma l}^{(\nu)}}\boldsymbol{d}_l^{(\nu)}, \tag{17}$$

where $\boldsymbol{d}_l^{(\nu)} = \phi_{\nu l}(t) * \boldsymbol{d}$, with $\nu = 2,\ 3,$ and 4. Similarly applying the Boltzmann operation to the non-deviatoric part $\mathrm{tr}(\boldsymbol{e}_l^{(1)})$, we get

$$\partial_t \mathrm{tr}(\boldsymbol{e}_l^{(1)}) = \phi_{1l}(0)\mathrm{tr}(\boldsymbol{e}) - \frac{1}{\tau_{\sigma l}^{(1)}}\mathrm{tr}(\boldsymbol{e}_l^{(1)}) \tag{18}$$

Using (17) and (18), The equations for the memory variables are expressed as

$$\partial_t e_{111}^{(\delta)} = \phi_{\delta 1}(0)(\epsilon_{11} - \bar{\epsilon}) - \frac{e_{111}^{(\delta)}}{\tau_\sigma^{(\delta)}} \tag{19a}$$

$$\partial_t e_{221}^{(\delta)} = \phi_{\delta 1}(0)(\epsilon_{22} - \bar{\epsilon}) - \frac{e_{221}^{(\delta)}}{\tau_\sigma^{(\delta)}} \tag{19b}$$

$$\partial_t e_{231} = \phi_{21}(0)\gamma_{23} - \frac{e_{231}}{\tau_\sigma^{(2)}} \tag{19c}$$

$$\partial_t e_{131} = \phi_{31}(0)\gamma_{13} - \frac{e_{131}}{\tau_\sigma^{(3)}} \tag{19d}$$

$$\partial_t e_{121} = \phi_{41}(0)\gamma_{12} - \frac{e_{121}}{\tau_\sigma^{(4)}} \tag{19e}$$

$$\partial_t e_{11} = n\phi_{1l}(0)\bar{\epsilon} - e_{11}/\tau_\sigma^{(1)} \tag{19f}$$

where $\bar{\epsilon} = tr(\boldsymbol{S})/3$ and n is taken as 2 for 2D and 3 for 3D.

2.5. Equation of motion

The conservation of momentum is expressed as

$$\frac{\partial \sigma_{11}}{\partial x_1} + \frac{\partial \sigma_{12}}{\partial x_2} + \frac{\partial \sigma_{13}}{\partial x_3} = \rho \frac{\partial v_1}{\partial t} \tag{20a}$$

$$\frac{\partial \sigma_{12}}{\partial x_1} + \frac{\partial \sigma_{22}}{\partial x_2} + \frac{\partial \sigma_{23}}{\partial x_3} = \rho \frac{\partial v_2}{\partial t} \tag{20b}$$

$$\frac{\partial \sigma_{13}}{\partial x_1} + \frac{\partial \sigma_{23}}{\partial x_2} + \frac{\partial \sigma_{33}}{\partial x_3} = \rho \frac{\partial v_3}{\partial t} \tag{20c}$$

3. Symmetrization of the anisotropic viscoelastic system

In this section, we show how to symmetrize the anisotropic viscoelastic wave equations introduced in subsections (2.1)-(2.4). In particular, anisotropic viscoelastic terms can be expressed using a symmetric and negative-definite matrix, which will enable us to construct a high order DG method which is provably energy dissipative for general frequency-dependent dissipative material properties.

Let us consider the 3D-particle-velocity and stress equations for propagation in an anisotropic medium. We assign one relaxation mechanism to both dilatational anelastic deformation ($\nu = 1$) and shear anelastic deformations ($\nu = 2$). The stress-strain relation is expressed as

$$
\begin{aligned}
\frac{\partial \sigma_{11}}{\partial t} &= c_{11}\frac{\partial v_1}{\partial x_1} + c_{12}\frac{\partial v_2}{\partial x_2} + c_{13}\frac{\partial v_3}{\partial x_3} + Ke_1 + 2Ge_2, \\
\frac{\partial \sigma_{22}}{\partial t} &= c_{12}\frac{\partial v_1}{\partial x_1} + c_{11}\frac{\partial v_2}{\partial x_2} + c_{13}\frac{\partial v_3}{\partial x_3} + Ke_1 + 2Ge_3, \\
\frac{\partial \sigma_{33}}{\partial t} &= c_{13}\frac{\partial v_1}{\partial x_1} + c_{13}\frac{\partial v_2}{\partial x_2} + c_{33}\frac{\partial v_3}{\partial x_3} + Ke_1 - 2G(e_2 + e_3) \\
\frac{\partial \sigma_{23}}{\partial t} &= c_{44}\left[\left(\frac{\partial v_2}{\partial x_3} + \frac{\partial v_3}{\partial x_2}\right) + e_4\right], \\
\frac{\partial \sigma_{13}}{\partial t} &= c_{55}\left[\left(\frac{\partial v_1}{\partial x_3} + \frac{\partial v_3}{\partial x_1}\right) + e_5\right], \\
\frac{\partial \sigma_{12}}{\partial t} &= c_{66}\left[\left(\frac{\partial v_1}{\partial x_2} + \frac{\partial v_2}{\partial x_1}\right) + e_6\right].
\end{aligned} \tag{21}
$$

Memory variables are expressed as

$$
\begin{aligned}
\frac{\partial e_1}{\partial t} &= \frac{1}{\tau_\sigma^{(1)}}\left[\left(\frac{\tau_\sigma^{(1)}}{\tau_\epsilon^{(1)}} - 1\right)\left(\frac{\partial v_1}{\partial x_1} + \frac{\partial v_2}{\partial x_2} + \frac{\partial v_3}{\partial x_3}\right) - e_1\right], \\
\frac{\partial e_2}{\partial t} &= \frac{1}{3\tau_\sigma^{(2)}}\left[\left(\frac{\tau_\sigma^{(2)}}{\tau_\epsilon^{(2)}} - 1\right)\left(2\frac{\partial v_1}{\partial x_1} - \frac{\partial v_2}{\partial x_2} - \frac{\partial v_3}{\partial x_3}\right) - 3e_2\right], \\
\frac{\partial e_3}{\partial t} &= \frac{1}{3\tau_\sigma^{(3)}}\left[\left(\frac{\tau_\sigma^{(3)}}{\tau_\epsilon^{(3)}} - 1\right)\left(2\frac{\partial v_2}{\partial x_2} - \frac{\partial v_1}{\partial x_1} - \frac{\partial v_3}{\partial x_3}\right) - 3e_3\right], \\
\frac{\partial e_4}{\partial t} &= \frac{1}{\tau_\sigma^{(2)}}\left[\left(\frac{\tau_\sigma^{(2)}}{\tau_\epsilon^{(2)}} - 1\right)\left(\frac{\partial v_2}{\partial x_3} + \frac{\partial v_3}{\partial x_2}\right) - e_4\right], \\
\frac{\partial e_5}{\partial t} &= \frac{1}{\tau_\sigma^{(3)}}\left[\left(\frac{\tau_\sigma^{(3)}}{\tau_\epsilon^{(3)}} - 1\right)\left(\frac{\partial v_1}{\partial x_3} + \frac{\partial v_3}{\partial x_1}\right) - e_5\right], \\
\frac{\partial e_6}{\partial t} &= \frac{1}{\tau_\sigma^{(4)}}\left[\left(\frac{\tau_\sigma^{(4)}}{\tau_\epsilon^{(4)}} - 1\right)\left(\frac{\partial v_1}{\partial x_2} + \frac{\partial v_2}{\partial x_1}\right) - e_6\right].
\end{aligned} \tag{22}
$$

Combining (20)-(22) in matrix form yields

$$
\frac{\partial \boldsymbol{q}}{\partial t} + \boldsymbol{A}(\boldsymbol{x})\frac{\partial \boldsymbol{q}}{\partial x_1} + \boldsymbol{B}(\boldsymbol{x})\frac{\partial \boldsymbol{q}}{\partial x_2} + \boldsymbol{C}(\boldsymbol{x})\frac{\partial \boldsymbol{q}}{\partial x_3} = \boldsymbol{D}(\boldsymbol{x})\boldsymbol{q} + \boldsymbol{f}, \tag{23}
$$

where

$$
\boldsymbol{q} = \left[\ \sigma_{11},\ \sigma_{22},\ \sigma_{33},\ \sigma_{23},\ \sigma_{13},\ \sigma_{12},\ e_1,\ e_2,\ e_3,\ e_4,\ e_5,\ e_6,\ v_1,\ v_2,\ v_3\ \right],
$$

.

$$\boldsymbol{A}(\boldsymbol{x}) = -\begin{bmatrix}
0 & 0 & 0 & 0 & 0 & 0 & 0 & 0 & 0 & 0 & 0 & 0 & c_{11}(\boldsymbol{x}) & 0 & 0 \\
0 & 0 & 0 & 0 & 0 & 0 & 0 & 0 & 0 & 0 & 0 & 0 & c_{12}(\boldsymbol{x}) & 0 & 0 \\
0 & 0 & 0 & 0 & 0 & 0 & 0 & 0 & 0 & 0 & 0 & 0 & c_{13}(\boldsymbol{x}) & 0 & 0 \\
0 & 0 & 0 & 0 & 0 & 0 & 0 & 0 & 0 & 0 & 0 & 0 & 0 & 0 & 0 \\
0 & 0 & 0 & 0 & 0 & 0 & 0 & 0 & 0 & 0 & 0 & 0 & 0 & 0 & c_{55}(\boldsymbol{x}) \\
0 & 0 & 0 & 0 & 0 & 0 & 0 & 0 & 0 & 0 & 0 & 0 & 0 & c_{66}(\boldsymbol{x}) & 0 \\
0 & 0 & 0 & 0 & 0 & 0 & 0 & 0 & 0 & 0 & 0 & 0 & T_1(\boldsymbol{x}) & 0 & 0 \\
0 & 0 & 0 & 0 & 0 & 0 & 0 & 0 & 0 & 0 & 0 & 0 & \frac{2}{3}T_2(\boldsymbol{x}) & 0 & 0 \\
0 & 0 & 0 & 0 & 0 & 0 & 0 & 0 & 0 & 0 & 0 & 0 & -\frac{1}{3}T_3(\boldsymbol{x}) & 0 & 0 \\
0 & 0 & 0 & 0 & 0 & 0 & 0 & 0 & 0 & 0 & 0 & 0 & 0 & 0 & 0 \\
0 & 0 & 0 & 0 & 0 & 0 & 0 & 0 & 0 & 0 & 0 & 0 & 0 & 0 & T_3(\boldsymbol{x}) \\
0 & 0 & 0 & 0 & 0 & 0 & 0 & 0 & 0 & 0 & 0 & 0 & 0 & T_4(\boldsymbol{x}) & 0 \\
1/\rho(\boldsymbol{x}) & 0 & 0 & 0 & 0 & 0 & 0 & 0 & 0 & 0 & 0 & 0 & 0 & 0 & 0 \\
0 & 0 & 0 & 0 & 0 & 1/\rho(\boldsymbol{x}) & 0 & 0 & 0 & 0 & 0 & 0 & 0 & 0 & 0 \\
0 & 0 & 0 & 0 & 1/\rho(\boldsymbol{x}) & 0 & 0 & 0 & 0 & 0 & 0 & 0 & 0 & 0 & 0
\end{bmatrix},$$

$$\boldsymbol{B}(\boldsymbol{x}) = -\begin{bmatrix}
0 & 0 & 0 & 0 & 0 & 0 & 0 & 0 & 0 & 0 & 0 & 0 & 0 & c_{12}(\boldsymbol{x}) & 0 \\
0 & 0 & 0 & 0 & 0 & 0 & 0 & 0 & 0 & 0 & 0 & 0 & 0 & c_{11}(\boldsymbol{x}) & 0 \\
0 & 0 & 0 & 0 & 0 & 0 & 0 & 0 & 0 & 0 & 0 & 0 & 0 & c_{13}(\boldsymbol{x}) & 0 \\
0 & 0 & 0 & 0 & 0 & 0 & 0 & 0 & 0 & 0 & 0 & 0 & 0 & 0 & c_{44}(\boldsymbol{x}) \\
0 & 0 & 0 & 0 & 0 & 0 & 0 & 0 & 0 & 0 & 0 & 0 & 0 & 0 & 0 \\
0 & 0 & 0 & 0 & 0 & 0 & 0 & 0 & 0 & 0 & 0 & 0 & c_{66}(\boldsymbol{x}) & 0 & 0 \\
0 & 0 & 0 & 0 & 0 & 0 & 0 & 0 & 0 & 0 & 0 & 0 & 0 & T_1(\boldsymbol{x}) & 0 \\
0 & 0 & 0 & 0 & 0 & 0 & 0 & 0 & 0 & 0 & 0 & 0 & 0 & -\frac{1}{3}T_2(\boldsymbol{x}) & 0 \\
0 & 0 & 0 & 0 & 0 & 0 & 0 & 0 & 0 & 0 & 0 & 0 & 0 & \frac{2}{3}T_3(\boldsymbol{x}) & 0 \\
0 & 0 & 0 & 0 & 0 & 0 & 0 & 0 & 0 & 0 & 0 & 0 & 0 & 0 & T_2(\boldsymbol{x}) \\
0 & 0 & 0 & 0 & 0 & 0 & 0 & 0 & 0 & 0 & 0 & 0 & 0 & 0 & 0 \\
0 & 0 & 0 & 0 & 0 & 0 & 0 & 0 & 0 & 0 & 0 & 0 & T_4(\boldsymbol{x}) & 0 & 0 \\
0 & 0 & 0 & 0 & 0 & 1/\rho(\boldsymbol{x}) & 0 & 0 & 0 & 0 & 0 & 0 & 0 & 0 & 0 \\
0 & 1/\rho(\boldsymbol{x}) & 0 & 0 & 0 & 0 & 0 & 0 & 0 & 0 & 0 & 0 & 0 & 0 & 0 \\
0 & 0 & 0 & 1/\rho(\boldsymbol{x}) & 0 & 0 & 0 & 0 & 0 & 0 & 0 & 0 & 0 & 0 & 0
\end{bmatrix},$$

$$\boldsymbol{C}(\boldsymbol{x}) = -\begin{bmatrix}
0 & 0 & 0 & 0 & 0 & 0 & 0 & 0 & 0 & 0 & 0 & 0 & 0 & 0 & c_{13}(\boldsymbol{x}) \\
0 & 0 & 0 & 0 & 0 & 0 & 0 & 0 & 0 & 0 & 0 & 0 & 0 & 0 & c_{13}(\boldsymbol{x}) \\
0 & 0 & 0 & 0 & 0 & 0 & 0 & 0 & 0 & 0 & 0 & 0 & 0 & 0 & c_{33}(\boldsymbol{x}) \\
0 & 0 & 0 & 0 & 0 & 0 & 0 & 0 & 0 & 0 & 0 & 0 & 0 & c_{44}(\boldsymbol{x}) & 0 \\
0 & 0 & 0 & 0 & 0 & 0 & 0 & 0 & 0 & 0 & 0 & 0 & c_{55}(\boldsymbol{x}) & 0 & 0 \\
0 & 0 & 0 & 0 & 0 & 0 & 0 & 0 & 0 & 0 & 0 & 0 & 0 & 0 & 0 \\
0 & 0 & 0 & 0 & 0 & 0 & 0 & 0 & 0 & 0 & 0 & 0 & 0 & 0 & T_1(\boldsymbol{x}) \\
0 & 0 & 0 & 0 & 0 & 0 & 0 & 0 & 0 & 0 & 0 & 0 & 0 & 0 & -\frac{1}{3}T_2(\boldsymbol{x}) \\
0 & 0 & 0 & 0 & 0 & 0 & 0 & 0 & 0 & 0 & 0 & 0 & 0 & 0 & \frac{2}{3}T_3(\boldsymbol{x}) \\
0 & 0 & 0 & 0 & 0 & 0 & 0 & 0 & 0 & 0 & 0 & 0 & 0 & T_2(\boldsymbol{x}) & 0 \\
0 & 0 & 0 & 0 & 0 & 0 & 0 & 0 & 0 & 0 & 0 & 0 & T_3(\boldsymbol{x}) & 0 & 0 \\
0 & 0 & 0 & 0 & 0 & 0 & 0 & 0 & 0 & 0 & 0 & 0 & 0 & 0 & 0 \\
0 & 0 & 0 & 0 & 1/\rho(\boldsymbol{x}) & 0 & 0 & 0 & 0 & 0 & 0 & 0 & 0 & 0 & 0 \\
0 & 0 & 0 & 1/\rho(\boldsymbol{x}) & 0 & 0 & 0 & 0 & 0 & 0 & 0 & 0 & 0 & 0 & 0 \\
0 & 0 & 1/\rho(\boldsymbol{x}) & 0 & 0 & 0 & 0 & 0 & 0 & 0 & 0 & 0 & 0 & 0 & 0
\end{bmatrix},$$

$$\boldsymbol{D}(\boldsymbol{x}) = -\begin{bmatrix}
0 & 0 & 0 & 0 & 0 & 0 & K(\boldsymbol{x}) & 2G(\boldsymbol{x}) & 0 & 0 & 0 & 0 & 0 & 0 & 0 \\
0 & 0 & 0 & 0 & 0 & 0 & K(\boldsymbol{x}) & 0 & 2G(\boldsymbol{x}) & 0 & 0 & 0 & 0 & 0 & 0 \\
0 & 0 & 0 & 0 & 0 & 0 & K(\boldsymbol{x}) & -2G(\boldsymbol{x}) & -2G(\boldsymbol{x}) & 0 & 0 & 0 & 0 & 0 & 0 \\
0 & 0 & 0 & 0 & 0 & 0 & 0 & 0 & 0 & c_{44}(\boldsymbol{x}) & 0 & 0 & 0 & 0 & 0 \\
0 & 0 & 0 & 0 & 0 & 0 & 0 & 0 & 0 & 0 & c_{55}(\boldsymbol{x}) & 0 & 0 & 0 & 0 \\
0 & 0 & 0 & 0 & 0 & 0 & 0 & 0 & 0 & 0 & 0 & c_{66}(\boldsymbol{x}) & 0 & 0 & 0 \\
0 & 0 & 0 & 0 & 0 & 0 & -\dfrac{1}{\tau_\sigma^{(1)}(\boldsymbol{x})} & 0 & 0 & 0 & 0 & 0 & 0 & 0 & 0 \\
0 & 0 & 0 & 0 & 0 & 0 & 0 & -\dfrac{1}{\tau_\sigma^{(2)}(\boldsymbol{x})} & 0 & 0 & 0 & 0 & 0 & 0 & 0 \\
0 & 0 & 0 & 0 & 0 & 0 & 0 & 0 & -\dfrac{1}{\tau_\sigma^{(3)}(\boldsymbol{x})} & 0 & 0 & 0 & 0 & 0 & 0 \\
0 & 0 & 0 & 0 & 0 & 0 & 0 & 0 & 0 & -\dfrac{1}{\tau_\sigma^{(2)}(\boldsymbol{x})} & 0 & 0 & 0 & 0 & 0 \\
0 & 0 & 0 & 0 & 0 & 0 & 0 & 0 & 0 & 0 & -\dfrac{1}{\tau_\sigma^{(3)}(\boldsymbol{x})} & 0 & 0 & 0 & 0 \\
0 & 0 & 0 & 0 & 0 & 0 & 0 & 0 & 0 & 0 & 0 & -\dfrac{1}{\tau_\sigma^{(4)}(\boldsymbol{x})} & 0 & 0 & 0 \\
0 & 0 & 0 & 0 & 0 & 0 & 0 & 0 & 0 & 0 & 0 & 0 & 0 & 0 & 0 \\
0 & 0 & 0 & 0 & 0 & 0 & 0 & 0 & 0 & 0 & 0 & 0 & 0 & 0 & 0 \\
0 & 0 & 0 & 0 & 0 & 0 & 0 & 0 & 0 & 0 & 0 & 0 & 0 & 0 & 0
\end{bmatrix},$$

where $T_i = \dfrac{1}{\tau_\sigma^{(i)}(\boldsymbol{x})}\left(\dfrac{\tau_\sigma^{(i)}(\boldsymbol{x})}{\tau_\epsilon^{(i)}(\boldsymbol{x})} - 1\right)$.

To prove stability of the scheme, we express (23) in a form where spatially dependent material coefficient appear on left side of (25). This will enable us to rewrite (22) without terms involving the spatial derivatives. From (21), we compute $\dfrac{\partial v_1}{\partial x_1}, \dfrac{\partial v_2}{\partial x_2}, \dfrac{\partial v_3}{\partial x_3}, \dfrac{\partial v_2}{\partial x_3}, \dfrac{\partial v_3}{\partial x_2}, \dfrac{\partial v_1}{\partial x_3}, \dfrac{\partial v_3}{\partial x_1}, \dfrac{\partial v_1}{\partial x_2}$, and $\dfrac{\partial v_2}{\partial x_1}$ and substitute in (22), which yields

$$\begin{aligned}
\frac{\partial a_1}{\partial t} &= -w_1(a_1 + z_1) - w_2(a_2 + z_2) - 2w_3(a_3 + z_3) \\
\frac{\partial a_2}{\partial t} &= w_4(a_1 + z_1) + w_5(a_2 + z_2) + 2w_6(a_3 + z_3) \\
\frac{\partial a_3}{\partial t} &= w_7(a_1 + z_1) + w_8(a_2 + z_2) + 2w_9(a_3 + z_3) \\
\frac{\partial a_4}{\partial t} &= T_2(a_4 + z_4) - \frac{(a_4 + z_4)}{\tau_\sigma^{(2)}} \\
\frac{\partial a_5}{\partial t} &= T_3(a_5 + z_5) - \frac{(a_5 + z_5)}{\tau_\sigma^{(3)}} \\
\frac{\partial a_6}{\partial t} &= T_4(a_6 + z_6) - \frac{(a_6 + z_6)}{\tau_\sigma^{(4)}},
\end{aligned} \tag{24}$$

where

$$\begin{aligned}
a_1 &= e_1 - z_1, \qquad a_2 = e_2 - z_2, \qquad a_3 = e_3 - z_3, \\
a_4 &= e_4 - z_4, \qquad a_5 = e_5 - z_5, \qquad a_6 = e_6 - z_6,
\end{aligned}$$

and

$$d_1 = r_{11} + r_{12} + r_{13}, \qquad d_2 = r_{33} + 2r_{13},$$

with r_{ij} being the elements of the inverse of unrelaxed compliance matrix

$$\boldsymbol{C}_p(\boldsymbol{x}) = \begin{bmatrix} c_{11}(\boldsymbol{x}) & c_{12}(\boldsymbol{x}) & c_{13}(\boldsymbol{x}) & 0 & 0 & 0 \\ c_{12}(\boldsymbol{x}) & c_{22}(\boldsymbol{x}) & c_{13}(\boldsymbol{x}) & 0 & 0 & 0 \\ c_{13}(\boldsymbol{x}) & c_{13}(\boldsymbol{x}) & c_{33}(\boldsymbol{x}) & 0 & 0 & 0 \\ 0 & 0 & 0 & c_{44}(\boldsymbol{x}) & 0 & 0 \\ 0 & 0 & 0 & 0 & c_{55}(\boldsymbol{x}) & 0 \\ 0 & 0 & 0 & 0 & 0 & c_{66}(\boldsymbol{x}) \end{bmatrix},$$

and inverse $\boldsymbol{C}_p$ is given in Appendix A.

$$\begin{aligned} z_1 &= T_1(d_1(\sigma_{11}+\sigma_{22}) + d_2\sigma_{33}), \\ z_2 &= T_2\left[\left(r_{11}-\frac{1}{3}d_1\right)\sigma_{11} + \left(r_{12}-\frac{1}{3}d_1\right)\sigma_{22} + \left(r_{13}-\frac{1}{3}d_2\right)\sigma_{33}\right], \\ z_3 &= T_3\left[\left(r_{12}-\frac{1}{3}d_1\right)\sigma_{11} + \left(r_{11}-\frac{1}{3}d_1\right)\sigma_{22} + \left(r_{13}-\frac{1}{3}d_2\right)\sigma_{33}\right], \\ z_4 &= T_2 c_{44}^{-1}\sigma_{23}, \qquad z_5 = T_3 c_{55}^{-1}\sigma_{13}, \qquad z_6 = T_4 c_{66}^{-1}\sigma_{12}, \end{aligned}$$

and

$$\begin{aligned} w_1 &= \left(T_1 p_\lambda + \frac{1}{\tau_\sigma^{(1)}}\right), & w_2 &= T_1 p_{\mu_1}, & w_3 &= T_1 p_{\mu_2}, \\ w_4 &= \left(\frac{T_2 p_\lambda}{3} - \frac{1}{\tau_\sigma^{(2)}} - K(r_{11}+r_{12})\right), & w_5 &= (T_2 p_{\mu_1} - G(r_{11}-r_{13})), & w_6 &= (T_2 p_{\mu_2} - G(r_{12}-r_{13})), \\ w_7 &= \left(\frac{T_3 p_\lambda}{3} - \frac{1}{\tau_\sigma^{(3)}} - K(r_{12}+r_{11})\right), & w_8 &= (T_3 p_{\mu_1} - G(r_{12}-r_{13})), & w_9 &= (T_3 p_{\mu_2} - G(r_{11}-r_{13})), \end{aligned}$$

with

$$p_\lambda = K(2d_1+d_2), \qquad p_{\mu_1} = G(d_1-2d_2), \qquad p_{\mu_2} = 2G(d_1-d_2).$$

We rewrite the system of equations (22) with out spatial derivative using the set of equations in (21), which yields

$$\begin{aligned} \boldsymbol{Q}_s^{-1}(\boldsymbol{x})\frac{\partial \boldsymbol{\sigma}}{\partial t} &= \sum_{i=1}^{d} \boldsymbol{A}_i \frac{\partial \boldsymbol{v}}{\partial \boldsymbol{x}_i} + \boldsymbol{S}\boldsymbol{\sigma}, \\ \rho\frac{\partial \boldsymbol{v}}{\partial t} &= \sum_{i=1}^{d} \boldsymbol{A}_i^T \frac{\partial \boldsymbol{\sigma}}{\partial \boldsymbol{x}_i} + \boldsymbol{f}, \end{aligned} \tag{25}$$

where, $\boldsymbol{\sigma} = [\sigma_{11},\ \sigma_{22},\ \sigma_{33},\ \sigma_{23}, \sigma_{13}, \sigma_{12},\ a_1,\ a_2,\ a_3,\ a_4,\ a_5,\ a_6]^T$, and $\boldsymbol{v} = [v_1,\ v_2,\ v_3]^T$ and

$$\boldsymbol{Q}_s^{-1}(\boldsymbol{x}) = \left[\begin{array}{c|c} \boldsymbol{C}_p^{-1}(\boldsymbol{x}) & \boldsymbol{0} \\ \hline \boldsymbol{0} & \boldsymbol{I} \end{array}\right].$$

The matrices $\boldsymbol{A}_i$ and $\boldsymbol{S}$ are

$$\boldsymbol{A}_1 = \left[\begin{array}{ccc} 1 & 0 & 0 \\ 0 & 0 & 0 \\ 0 & 0 & 0 \\ 0 & 0 & 0 \\ 0 & 0 & 1 \\ 0 & 1 & 0 \\ \hline 0 & 0 & 0 \\ 0 & 0 & 0 \\ 0 & 0 & 0 \\ 0 & 0 & 0 \\ 0 & 0 & 0 \\ 0 & 0 & 0 \end{array}\right], \qquad \boldsymbol{A}_2 = \left[\begin{array}{ccc} 0 & 0 & 0 \\ 0 & 1 & 0 \\ 0 & 0 & 0 \\ 0 & 0 & 1 \\ 0 & 0 & 0 \\ 1 & 0 & 0 \\ \hline 0 & 0 & 0 \\ 0 & 0 & 0 \\ 0 & 0 & 0 \\ 0 & 0 & 0 \\ 0 & 0 & 0 \\ 0 & 0 & 0 \end{array}\right], \qquad \boldsymbol{A}_3 = \left[\begin{array}{ccc} 0 & 0 & 0 \\ 0 & 0 & 0 \\ 0 & 0 & 1 \\ 0 & 1 & 0 \\ 1 & 0 & 0 \\ 0 & 0 & 0 \\ \hline 0 & 0 & 0 \\ 0 & 0 & 0 \\ 0 & 0 & 0 \\ 0 & 0 & 0 \\ 0 & 0 & 0 \\ 0 & 0 & 0 \end{array}\right],$$

and $\boldsymbol{S} = \boldsymbol{Q}_s^{-1}\boldsymbol{G}$ with

$$\boldsymbol{G} = \left[\begin{array}{c|c} \boldsymbol{g}11_{6\times 6} & \boldsymbol{g}12_{6\times 6} \\ \hline \boldsymbol{g}21_{6\times 6} & \boldsymbol{g}22_{6\times 6} \end{array}\right]$$

where

$$\boldsymbol{g}_{11} = \begin{bmatrix} T_1 d_1 + 2GT_2 g_1 & KT_1 d_1 + 2GT_2 g_2 & KT_1 d_2 + 2GT_2 g_3 & 0 & 0 & 0 \\ KT_1 d_1 + 2GT_3 g_4 & KT_1 d_1 + 2GT_3 g_5 & KT_1 d_2 + 2GT_3 g_6 & 0 & 0 & 0 \\ KT_1 d_1 - 2Gg_7 & KT_1 d_1 - 2Gg_8 & KT_1 d_2 - 2Gg_9 & 0 & 0 & 0 \\ 0 & 0 & 0 & T_2 c_{44}^{-1} & 0 & 0 \\ 0 & 0 & 0 & 0 & T_3 c_{55}^{-1} & 0 \\ 0 & 0 & 0 & 0 & 0 & T_4 c_{66}^{-1} \end{bmatrix},$$

$$\boldsymbol{g}_{12} = \begin{bmatrix} K & 2G & 0 & 0 & 0 & 0 \\ K & 0 & 2G & 0 & 0 & 0 \\ K & -2G & -2G & 0 & 0 & 0 \\ 0 & 0 & 0 & c_{44} & 0 & 0 \\ 0 & 0 & 0 & 0 & c_{55} & 0 \\ 0 & 0 & 0 & 0 & 0 & c_{66} \end{bmatrix},$$

$$\boldsymbol{g}_{21} = \begin{bmatrix} t_1 & t_2 & t_3 & 0 & 0 & 0 \\ t_4 & t_5 & t_6 & 0 & 0 & 0 \\ t_7 & t_8 & t_9 & 0 & 0 & 0 \\ 0 & 0 & 0 & \left(T_2 - \dfrac{1}{\tau_\sigma^{(2)}}\right) T_2/c_{44} & 0 & 0 \\ 0 & 0 & 0 & 0 & \left(T_3 - \dfrac{1}{\tau_\sigma^{(3)}}\right) T_3/c_{55} & 0 \\ 0 & 0 & 0 & 0 & 0 & \left(T_4 - \dfrac{1}{\tau_\sigma^{(4)}}\right) T_4/c_{66} \end{bmatrix},$$

$$\boldsymbol{g}_{22} = \begin{bmatrix} -w_1 & -w_2 & w_3 & 0 & 0 & 0 \\ w_4 & w_5 & w_6 & 0 & 0 & 0 \\ w_7 & w_8 & w_9 & 0 & 0 & 0 \\ 0 & 0 & 0 & \left(T_2 - \dfrac{1}{\tau_\sigma^{(2)}}\right) & 0 & 0 \\ 0 & 0 & 0 & 0 & \left(T_3 - \dfrac{1}{\tau_\sigma^{(3)}}\right) & 0 \\ 0 & 0 & 0 & 0 & 0 & \left(T_4 - \dfrac{1}{\tau_\sigma^{(4)}}\right) \end{bmatrix}$$

where

$$g_1 = \left(r_{11} - \frac{1}{3}d_1\right), \quad g_2 = \left(r_{12} - \frac{1}{3}d_1\right), \quad g_3 = \left(r_{13} - \frac{1}{3}d_2\right),$$
$$g_4 = \left(r_{12} - \frac{1}{3}d_1\right), \quad g_5 = \left(r_{11} - \frac{1}{3}d_1\right), \quad g_6 = \left(r_{13} - \frac{1}{3}d_2\right),$$
$$g_7 = T_2 g_1 + T_3 g_4, \quad g_8 = T_2 g_2 + T_3 g_5, \quad g_9 = T_2 g_3 + T_3 g_6,$$
$$t_1 = -(w_1 T_1 d_1 + w_2 T_2 g_1 + 2w_3 T_3 g_4), \quad t_2 = -(w_1 T_1 d_1 + w_2 T_2 g_2 + 2w_3 g_5),$$
$$t_3 = -(w_1 T_1 d_2 + w_2 T_2 g_3 + 2w_3 g_6), \quad t_4 = w_4 T_1 d_1 + w_5 T_2 g_1 + 2w_6 T_3 g_4,$$
$$t_5 = w_4 T_1 d_1 + w_5 T_2 g_2 + 2w_6 g_5, \quad t_6 = w_4 T_1 d_2 + w_5 T_2 g_3 + 2w_6 g_6,$$
$$t_7 = w_7 T_1 d_1 + w_8 T_2 g_1 + 2w_9 T_3 g_4, \quad t_8 = w_7 T_1 d_1 + w_8 T_2 g_2 + 2w_9 g_5,$$
$$t_9 = w_7 T_1 d_2 + w_8 T_2 g_3 + 2w_9 g_6.$$

Here elements of $\boldsymbol{G}$ and $\boldsymbol{g}_{ij}$ are space dependent.

In (22), matrices $\boldsymbol{A}_i$ are spatially constant, where as $\boldsymbol{Q}_s^{-1}$ and ρ can vary spatially. We will also assume that ρ , $\boldsymbol{Q}_s^{-1}$ and $\boldsymbol{Q}_s^{-1}$ are positive-definite and bounded pointwise such that

$$0 < \rho_{\min} \leqslant \rho(\boldsymbol{x}) \leqslant \rho_{\max} < \infty$$
$$0 < c_{\min} \leqslant \boldsymbol{u}^T \boldsymbol{Q}_s(\boldsymbol{x}) \boldsymbol{u} \leqslant c_{\max} < \infty$$
$$0 < \hat{c}_{\min} \leqslant \boldsymbol{u}^T \boldsymbol{Q}_s^{-1}(\boldsymbol{x}) \boldsymbol{u} \leqslant \hat{c}_{\max} < \infty$$

for all $\boldsymbol{x} \in \mathbb{R}^d$ and $\forall\ \boldsymbol{u} \in \mathbb{R}^{N_d}$.
Moreover, we assume that $\boldsymbol{S}$ is a semi negative-definite and bounded pointwise such that

$$-\infty < s_{min} \leqslant \boldsymbol{s}^T \boldsymbol{S} \boldsymbol{s} \leqslant s_{max} < 0 \qquad \forall\ \boldsymbol{x} \in \mathbb{R}^d \text{ and } \forall\ \boldsymbol{u} \in \mathbb{R}^{N_d}.$$

4. An energy stable discontinuous Galerkin formulation for the viscoelastic wave equation

In this section, we formulate the energy stable discontinuous Galerkin methods for viscoelastic wave equation (25). We will first introduce the definitions and notations that will be used in subsequent subsections.

4.1. Notations and definitions for DG

We consider that domain Ω is exactly discretized by a mesh and represented by $\Omega_h = \bigcup_{k=1}^{K} \boldsymbol{D}^k$. The Ω_h is consist of non-overlapping elements D^k, which are images of a reference element $\widehat{D}$ under a local affine mapping defined as

$$\boldsymbol{x}^k = \Phi^k \widehat{\boldsymbol{x}}, \qquad \boldsymbol{x}^k \in D^k, \qquad \widehat{\boldsymbol{x}} \in \widehat{D}.$$

Here $\boldsymbol{x}^k = \{x^k, y^k\}$ for $d = 2$ and $\boldsymbol{x}^k = \{x^k, y^k, z^k\}$ for $d = 3$ denote the physical coordinates on element D^k and $\hat{\boldsymbol{x}} = \{\hat{x}, \hat{y}\}$ for $d = 2$ and $\hat{\boldsymbol{x}} = \{\hat{x}, \hat{y}, \hat{z}\}$ for $d = 3$ denote coordinates on the reference element, which is a bi-unit right angle. Over each element D^k, local approximation space $V_h(D^k)$ is defined as

$$V_h(D^k) = V_h(\widehat{D}) \circ \left(\Phi^k\right)^{-1} = \{\widehat{v}_h \circ (\Phi^k)^{-1}, \widehat{v}_h \in V_h(\widehat{D})\}.$$

The $V_h(\widehat{D})$ is local polynomial approximation space defined in 3D by

$$V_h(\widehat{D}) = P^N(\widehat{D}) = \{\hat{x}^i \hat{y}^j \hat{x}^k, 0 \leqslant i + j + k \leqslant N\},$$

with $P^N(\widehat{D})$ being the space of polynomials of total degree N on the reference simplex.

The L^2 inner product between two real vector-valued functions $\boldsymbol{g}$ and $\boldsymbol{h}$ over D^k and ∂D^k is expressed as

$$(\boldsymbol{g}, \boldsymbol{h}) = \int_{D^k} \boldsymbol{g} \cdot \boldsymbol{h} \; d\boldsymbol{x}, \qquad \langle \boldsymbol{g}, \boldsymbol{h} \rangle_{L^2(\partial D^k)} = \int_{\partial D^k} \boldsymbol{g} \cdot \boldsymbol{h} \; d\boldsymbol{x}$$

The jump and average of a scalar function $u \in V_h(\Omega_h)$ across faces of the elements are defined as

$$[\![u]\!] = u^+ - u^-, \qquad \{\{u\}\} = \frac{u^+ + u^-}{2},$$

where superscripts "+" and "-" represent neighboring and local traces of solutions over each faces of the element. Jumps and averages of vector-valued functions $\boldsymbol{u} \in \mathbb{R}^m$ and and matrix-valued functions $\tilde{\boldsymbol{S}} \in \mathbb{R}^{m \times n}$ are defined component-wise.

$$([\![\boldsymbol{u}]\!])_i = [\![\boldsymbol{u}_i]\!], \qquad 1 \leqslant i \leqslant m \qquad \left([\![\tilde{\boldsymbol{S}}]\!]\right)_{ij} = [\![\tilde{\boldsymbol{S}}]\!]$$

4.2. DG formulation

The DG formulation of (25) in strong form with penalty based numerical fluxes is expressed as [38]

$$\begin{aligned}
\sum_{D^k \in \Omega_h} \left(\boldsymbol{Q}_s^{-1} \frac{\partial \boldsymbol{\sigma}}{\partial t}, \boldsymbol{h} \right)_{L^2(D^k)} &= \sum_{D^k \in \Omega_h} \left(\left(\sum_{i=1}^{d} \boldsymbol{A}_i \frac{\partial \boldsymbol{v}}{\partial \boldsymbol{x}_i}, \boldsymbol{h} \right)_{L^2(D^k)} + \left\langle \frac{1}{2} \boldsymbol{A_n} [\![\boldsymbol{v}]\!] + \frac{\alpha_{\boldsymbol{\sigma}}}{2} \boldsymbol{A_n} \boldsymbol{A}_n^T [\![\boldsymbol{\sigma}]\!], \boldsymbol{h} \right\rangle_{L^2(\partial D^k)} \right. \\
&\qquad \left. + (\boldsymbol{S}\boldsymbol{\sigma}, \boldsymbol{g})_{L^2(D^k)} \right) \\
\sum_{D^k \in \Omega_h} \left(\rho \frac{\partial \boldsymbol{v}}{\partial t}, \boldsymbol{g} \right)_{L^2(D^k)} &= \sum_{D^k \in \Omega_h} \left(\left(\sum_{i=1}^{d} \boldsymbol{A}_i{}^T \frac{\partial \boldsymbol{\sigma}}{\partial \boldsymbol{x}_i} + \boldsymbol{f}, \boldsymbol{g} \right)_{L^2(D^k)} + \left\langle \frac{1}{2} \boldsymbol{A}_{\boldsymbol{n}}^T [\![\boldsymbol{\sigma}]\!] + \frac{\alpha_{\boldsymbol{v}}}{2} \boldsymbol{A}_n^T \boldsymbol{A_n} [\![\boldsymbol{v}]\!], \boldsymbol{g} \right\rangle_{L^2(\partial D^k)} \right),
\end{aligned} \tag{26}$$

for all $\boldsymbol{h},\ \boldsymbol{g} \in V_h(\Omega_h)$. Here, $\boldsymbol{A}_n$ is the normal matrix defined on a face of an element and expressed as

$$\boldsymbol{A}_n = \sum_{i=1}^{d} n_i \boldsymbol{A}_i = \left[\begin{array}{ccc}
n_x & 0 & 0 \\
0 & n_y & 0 \\
0 & 0 & n_z \\
0 & n_z & n_y \\
n_z & 0 & n_x \\
n_y & n_x & 0 \\
\hline
0 & 0 & 0 \\
0 & 0 & 0 \\
0 & 0 & 0 \\
0 & 0 & 0 \\
0 & 0 & 0 \\
0 & 0 & 0
\end{array}\right].$$

The factors $\alpha_\tau,\ \alpha_v(\geqslant 0)$ are penalty parameters, which are piecewise constant. These parameters are defined on the faces of the element. A non-dissipative central flux is recovered by choosing $\alpha_\tau,\ \alpha_v = 0$ whereas choosing $\alpha_\tau,\ \alpha_v > 0$ results into energy dissipation similar to the upwind flux [27, 39, 41]. In this work, we take $\alpha_\tau = \alpha_v = 1/2$ unless stated otherwise. A detail study on choice of penalty parameter and it's effect on time step is presented by Chan [37]. The semi-discrete matrix representation for DG formulation in (26) could be easily followed from [39, 41].

4.3. Energy stability

In the absence of external forces ($\boldsymbol{f} = 0$) and for free-surface and absorbing boundary conditions, the DG formulation in (26) can be proven to be energy stable by following the works of [41, 39]. The proof is straightforward using the techniques from [41, 39], and we do not include it for brevity. Thus the stability condition for DG formulation in (26) is stated as follows.

Theorem 1. *The DG formulation in (26) is energy stable for $\alpha_{\boldsymbol{\sigma}}, \alpha_{\boldsymbol{v}} \geqslant 0$ such that*

$$\begin{aligned}\sum_{D^k\in\Omega_h} \frac{1}{2}\frac{\partial}{\partial t}\left((\boldsymbol{Q}_s^{-1}\boldsymbol{\sigma},\boldsymbol{\sigma})_{L^2(D^k)} + (\boldsymbol{\rho}\boldsymbol{v},\boldsymbol{v})_{L^2(D^k)}\right) = &- \sum_{f\in\Gamma_h\setminus\partial\Omega}\int_f \left(\frac{\alpha_{\boldsymbol{\sigma}}}{2}\left|\boldsymbol{A}_n^T[\![\boldsymbol{\sigma}]\!]\right|^2 + \frac{\alpha_{\boldsymbol{v}}}{2}\left|\boldsymbol{A}_n[\![\boldsymbol{v}]\!]\right|^2\right) d\boldsymbol{x} \\ - \sum_{f\in\Gamma_{\boldsymbol{\sigma}}}\int_f \left(\alpha_{\boldsymbol{\sigma}}\left|\boldsymbol{A}_n^T\boldsymbol{\sigma}^-\right|^2\right)\ d\boldsymbol{x} &- \sum_{f\in\Gamma_{abc}}\int_f \left(\frac{\alpha_{\boldsymbol{\sigma}}}{2}\left|\boldsymbol{A}_n^T\boldsymbol{\sigma}^-\right|^2 + \frac{\alpha_{\boldsymbol{v}}}{2}\left|\boldsymbol{A}_n\boldsymbol{v}^-\right|^2\right) d\boldsymbol{x} \\ + \sum_{D^k\in\Omega_h}\int_{D^k} \boldsymbol{v}^T\boldsymbol{S}\boldsymbol{v}\ d\boldsymbol{x} &\leqslant 0. \end{aligned} \tag{27}$$

The term on the left hand side of (27) is an L^2-equivalent norm on $(\boldsymbol{\sigma},\boldsymbol{v})$ as $\boldsymbol{Q}_s^{-1}$ and ρ are positive definite. We can easily imply from Theorem 1 that magnitude of the DG solution is non-increasing in time and for $\alpha_{\boldsymbol{\tau}}, \alpha_{\boldsymbol{v}} \geqslant 0$ dissipation is present in the scheme.

5. Numerical experiments

In this section, we provide the stability and accuracy of the DG scheme in (26) in two and three dimensions by presenting several numerical experiments. This section also includes the confirmation of convergence of the scheme for an isotropic viscoelastic media with material properties being piecewise constant. In subsequent examples, the time integration is performed using the low-storage 4^{th} order five-stage Runge-Kutta scheme [42], with the time step dt expressed as

$$dt = \min_k \frac{C_{CFL}}{\max\left(\lambda_i\right) C_N \left\|J^f\right\|_{L^\infty(\partial D^k)} \left\|J^{-1}\right\|_{L^\infty(D^k)}} \tag{28}$$

where λ_i are wave speeds of the system [26], $C_N = O(N^2)$ with N being the order of scheme. C_{CFL} is a global CFL constant.The dt in (28) a very conservative estimate [37]. Moreover, due to presence of attenuation in viscoelastic system, the wave speeds are less than those present in the elastic wave equation, which results into slightly larger dt required for satisfying the CFL condition.

5.1. Spectra and choice of penalty parameter

The energy stability of proposed DG formulation is verified by computing the eigenvalues of matrix $\boldsymbol{A}_h$ induced by the global semi-discrete DG formulation. The semi-discrete representation of DG formulation (26) is expressed as

$$\frac{\partial \boldsymbol{q}}{\partial t} = \boldsymbol{A}_h\boldsymbol{q},$$

where $\boldsymbol{q}$ denotes a vector of global degrees of freedom. Eigenvalues of $\boldsymbol{A}_h$ for $\alpha = 0$ and $\alpha = 1$ in an isotropic sandstone (Column 3 of Table 1) are shown in Figure 1. Results in Figure 1 are computed with discretization

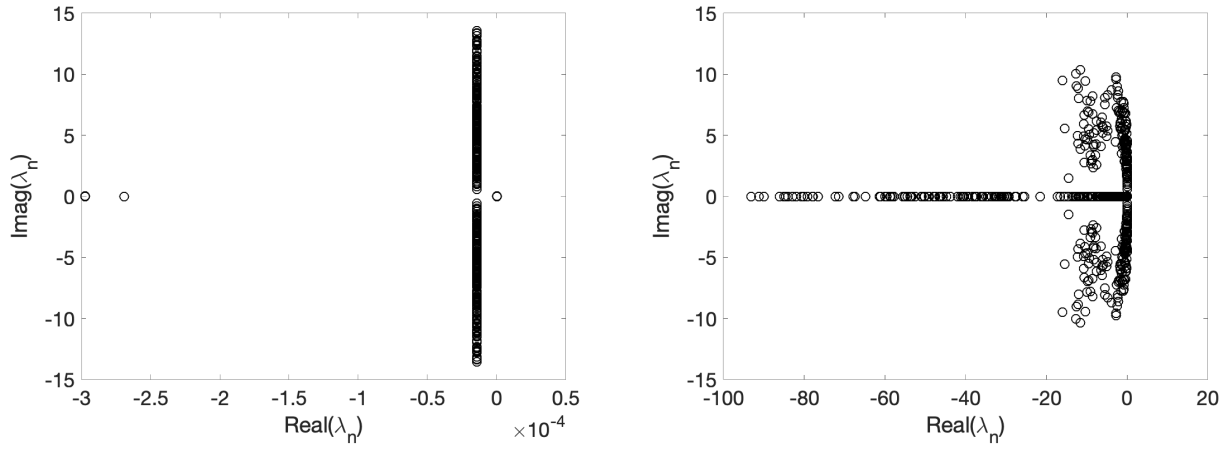

(a) $\alpha = 0$, central flux

(b) $\alpha = 1$, penalty flux

Figure 1: Spectra for isotropic Sandstone (Column 3 of Table 1) with $N = 3$ and $h = 1/2$. Largest real part of spectra $\lambda_{\max} = 1.83519\text{e}-14$ with $\alpha_\tau = \alpha_v = 0$ and $\lambda_{\max} = 2.18232\text{e}-14$ with $\alpha_\tau = \alpha_v = 1$.

Table 1: Material properties of anisotropic-viscoelastic media [7]

Properties	Clay shale	Phenolic	Isotropic Sandstone
Elasticities			
ρ_s (kg/m^3)	2590	1364	2500
c_{11} (GPa)	66.6	11.7	25.6
c_{12} (GPa)	19.7	6.7	9.4
c_{13} (GPa)	39.4	7.0	9.4
c_{22} (GPa)	66.6	15.4	25.6
c_{23} (GPa)	39.4	7.0	9.4
c_{33} (GPa)	39.9	17.4	25.6
c_{44} (GPa)	10.9	3.8	16.2
c_{55} (GPa)	10.9	3.5	16.2
c_{66} (GPa)	23.4	3.1	16.2
Relaxation time (s)			
$\tau_\epsilon^{(1)}$	8.00×10^{-3}	6.4×10^{-3}	$3.72 \times 10^{-}3$
$\tau_\sigma^{(1)}$	7.49×10^{-3}	6.00×10^{-3}	$3.36 \times 10^{-}3$
$\tau_\epsilon^{(2)}$	8.00×10^{-3}	6.4×10^{-3}	$3.78 \times 10^{-}3$
$\tau_\sigma^{(2)}$	7.25×10^{-3}	5.80×10^{-3}	$3.30 \times 10^{-}3$
$\tau_\epsilon^{(3)}$	8.00×10^{-3}	6.4×10^{-3}	$3.78 \times 10^{-}3$
$\tau_\sigma^{(3)}$	7.25×10^{-3}	5.60×10^{-3}	$3.30 \times 10^{-}3$
$\tau_\epsilon^{(4)}$	8.00×10^{-3}	6.4×10^{-3}	$3.78 \times 10^{-}3$
$\tau_\sigma^{(4)}$	7.25×10^{-3}	5.30×10^{-3}	$3.30 \times 10^{-}3$

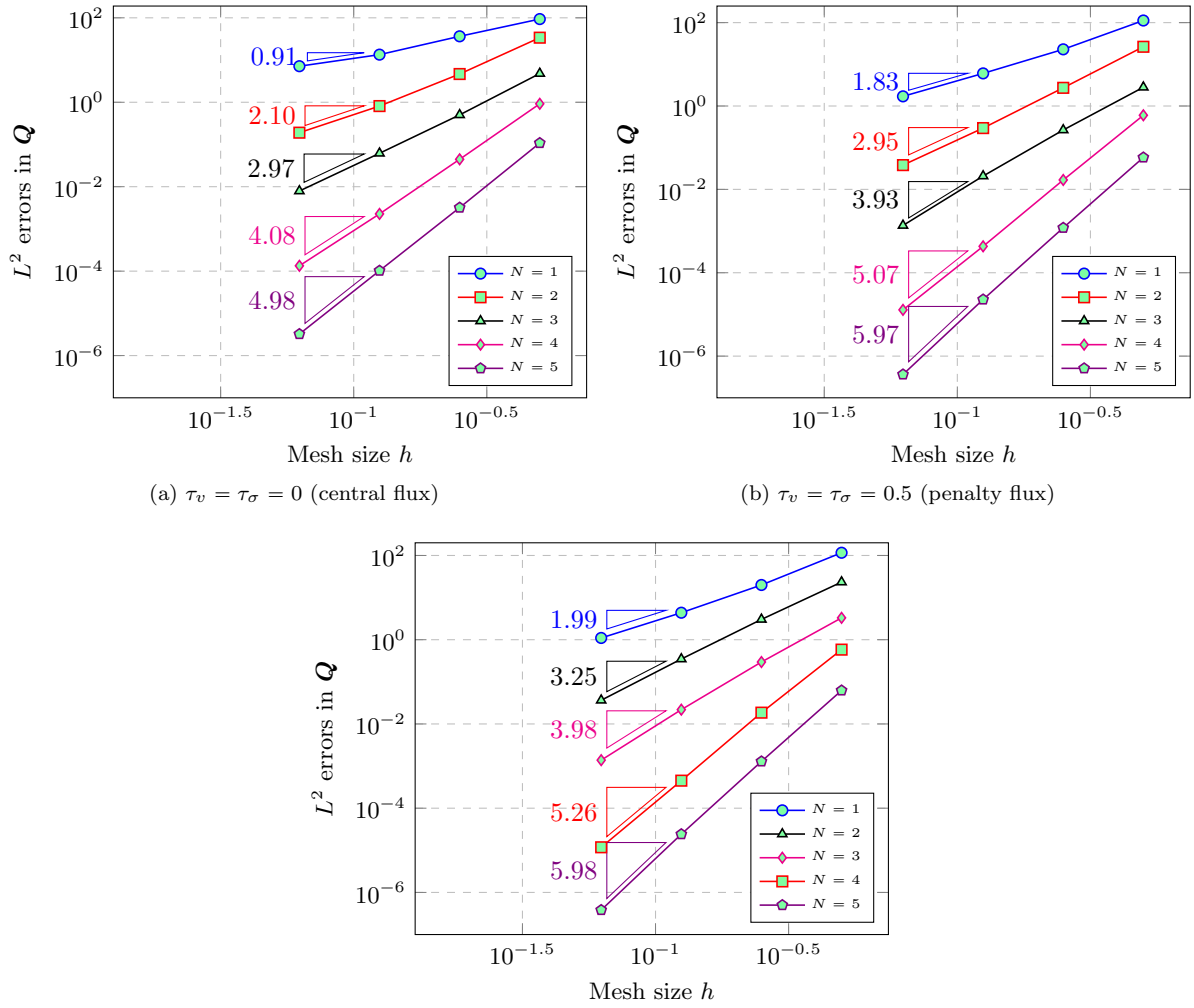

(a) $\tau_v = \tau_\sigma = 0$ (central flux)

(b) $\tau_v = \tau_\sigma = 0.5$ (penalty flux)

(c) $\tau_v = \tau_\sigma = 1$ (penalty flux)

Figure 2: Convergence of L^2 error for plane wave in a viscoelastic media

parameters of $N = 3$ and mesh size of $h = 1/2$. For both sets of penalty parameters, the largest value of real part of any eigenvalues is $O(10^{-14})$, which proves energy stability of the semi-discrete scheme. It is to be also noted that some eigenvalues for $\alpha = 0$ have purely negative real part, corresponding to the dissipation present in viscoelastic system.

An efficient DG scheme based on penalty fluxes requires that the selection of penalty parameters α should ensure that the magnitude of the spectral radius for $\alpha > 0$ is of the same order as the case when $\alpha = 0$ [37, 41]. For example, in isotropic Sandstone and for $\alpha = 0$, the spectral radius $\rho(\boldsymbol{A}_h)$ is 13.5653 which is $O(N^2/h)$. However, $\rho(\boldsymbol{A}_h)$ for $\alpha_{\boldsymbol{\tau}}, \alpha_{\boldsymbol{v}} = 0.5$ and $\alpha_{\boldsymbol{\tau}}, \alpha_{\boldsymbol{v}} = 1$ are 45.6388 $[O(N^2/h)]$ and 93.1184 $[O(N^2/h)]$, respectively. This also confirms that the choice of α for viscoelastic wave equation should be based on the same guiding principles as for the cases of acoustic [37], elastic [33, 39] and poroelastic wave equation [41].

5.2. Convergence for a plane wave in viscoelastic medium

The analytical solution to (23) for a plane wave is given as

$$\boldsymbol{q}(\boldsymbol{x}, t) = \boldsymbol{q}^0 \exp[\mathrm{i} \cdot (\omega t - \boldsymbol{k} \cdot \boldsymbol{x})] \tag{29}$$

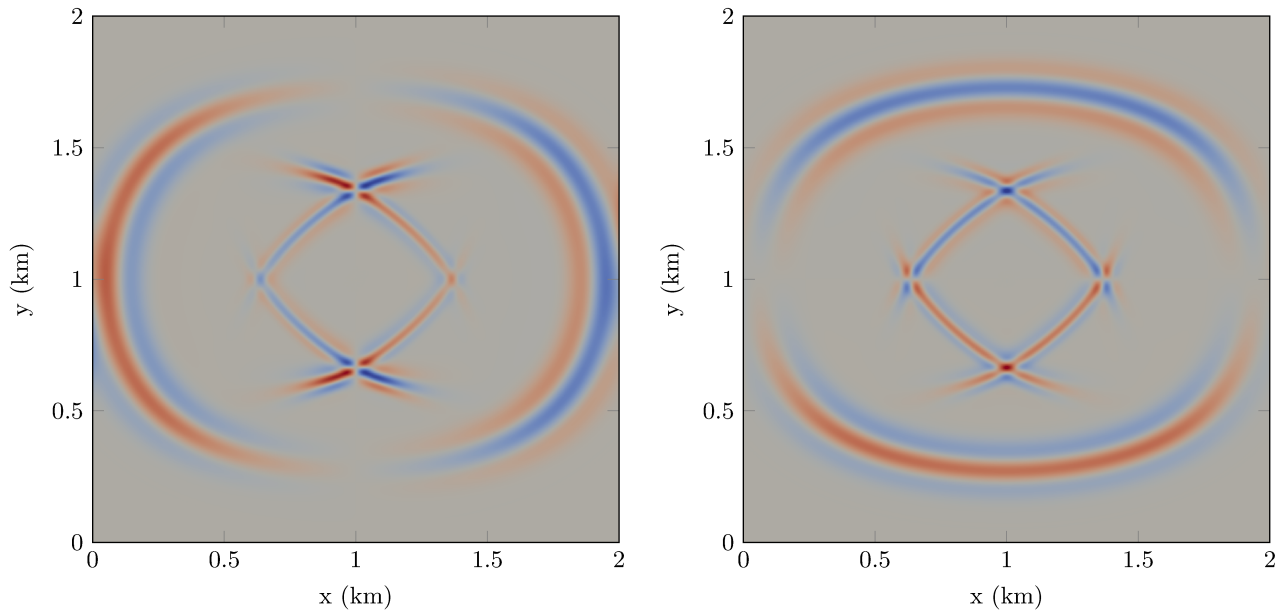

(a) Orthotropic shale, v_1

(b) Orthotropic shale, v_3

Figure 3: Snapshots of particle velocities in orthotropic shale (column 1 of Table 1), computed at $t = 0.22$ s, where (a) and (b) corresponds to v_1 and v_3 components. The central frequency of the forcing function is 20 Hz corresponding to the relaxation peak of materials. The point source is located in the center of the domain. The solution is computed using polynomials of degree $N = 3$ and $K = 32,768$.

where $\boldsymbol{q}^0$ is the initial amplitude of stress and velocity components; ω are wave frequencies; $\boldsymbol{k}$ is the wavevector defining the direction of wave propagation.

To incorporate all the wave modes present in viscoelastic system, we superimpose two plane waves (P and S waves) of the form expressed by (29). The computation of wave frequencies ω is performed by following the approach presented by Toro [43].

To study the accuracy and convergence of proposed numerical scheme (26), we computed relative L^2 errors between actual and numerical solution of all components of $\boldsymbol{q}$ corresponding to a plane wave in an isotropic sandstone (Table 1 and Column 3). The L^2 error is expressed as

$$\frac{\|\boldsymbol{q} - \boldsymbol{q}_h\|_{L^2(\Omega)}}{\|\boldsymbol{q}\|_{L^2(\Omega)}} = \frac{\left(\sum_{i=1}^{m} \|\boldsymbol{q_i} - \boldsymbol{q_{i,h}}\|^2_{L^2(\Omega)}\right)^{1/2}}{\left(\sum_{i=1}^{m} \|\boldsymbol{q_i}\|^2_{L^2(\Omega)}\right)^{1/2}}.$$

We show L^2 errors in Figure 2 which is computed for monochromatic plane waves at $T = 1$. To compute the error, we discretized the domain using uniform triangular meshes. Figure 2a shows error plots for $\alpha = 0$ (CFL = 1) (the central flux). The convergence rates of $O(h^N)$ or $O(h^{N+1})$ are observed for odd-even N, respectively. The convergence plots for $\alpha = 0.5$ (CFL = 0.5), and 1 (CFL = 0.8) with $N = 1, ..., 5$ are shown in Figure 2a and 2b. Figure 2a and 2b depict convergence rate of $O(h^{N+1})$ and confirms with theoretical convergence rate [27].

5.3. Application examples

In this section, we present physics of the waves propagation in linear and isotropic viscoelastic materials computed from presented DG scheme in (26). Results presented in this section accurately resolves the two types of elastic waves, P or longitudinal waves and shear or S waves, exhibiting anisotropic dissipative phenomena as they propagate in the medium.

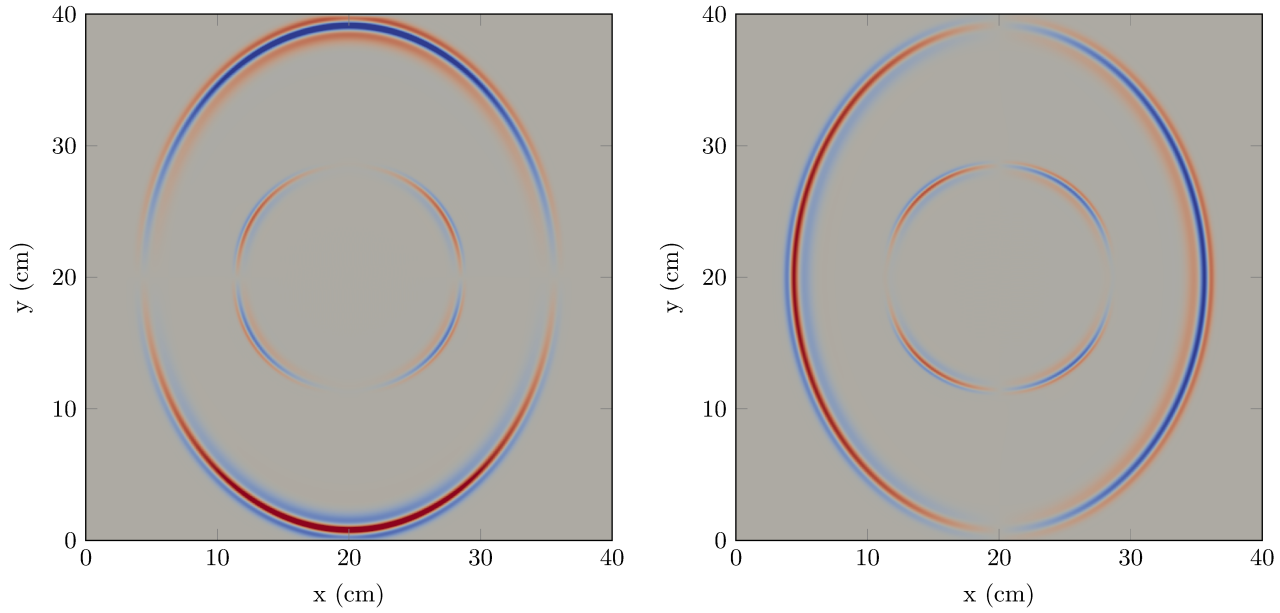

(a) Phenolic type material, v_1

(b) Phenolic type material, v_2

Figure 4: Snapshots of particle velocities in Phenolic material (column 2 of Table 1), computed at $t = 53.2$ μs, where (a) and (b) corresponds to v_1 and v_2 components. The central frequency of the forcing function (f_0) is 250 kHz which also corresponds to relaxation peak of the material. The point source is located in the center of the domain. The solution is computed using polynomials of degree $N = 3$ and $K = 131,072$.

In following examples, forcing functions are applied to both the horizontal and vertical components of stress i.e. $(\sigma_{11}, \sigma_{33})$. The forcing function are expressed as

$$f(\boldsymbol{x}, t) = (1 - 2(\pi f_0(t - t_0))^2) \exp[-(\pi f_0(t - t_0))^2]\delta(\boldsymbol{x} - \boldsymbol{x}_0), \tag{30}$$

where $\boldsymbol{x}_0$ is the location of the point source and f_0 is the central frequency and δ is Dirac-delta function.

5.3.1. 2D Orthotropic shale

To illustrate the effect of anisotropic dissipation in a viscoelastic medium, we perform a computational experiment in orthotropic shale with material properties given in Table 1 (Column 1). The size of the computational domain is 2 km × 2 km. The domain is discretized with uniform triangular elements with a minimum edge length of 15.625 m. Figures 3(a)-(b) show the $x-$ and $z-$ components of the particle velocity of the orthotropic shale, respectively. The central frequency of the forcing function is $f_0 = 20$ Hz, which is also the frequency for relaxation peak of the material. Polynomials of degree $N = 3$ are used for the simulation, and the propagation time is 0.22 s. Both wave modes can be observed: the P mode and the shear mode (S, inner wavefront). A shear wave cusp is clearly observed in Figure 3a and 3b.

5.3.2. 2D Phenolic material

To further validate our numerical scheme, we perform a computational experiment in Phenolic material which has a high relaxation frequency of 250 kHz with material properties given in Table 1 (Column 2). The size of the computational domain is 40 cm × 40 cm. The domain is discretized with uniform triangular elements with a minimum edge length of 0.1562 cm. Figures 4(a)-(b) represent the $x-$ and $z-$ components of the particle velocity of the Phenolic material, respectively. The central frequency of the forcing function is $f_0 = 250$ kHz (the frequency for relaxation peak). Polynomials of degree $N = 3$ are used for the simulation. The propagation time is 53.2 μs. Both modes of waves can be observed.

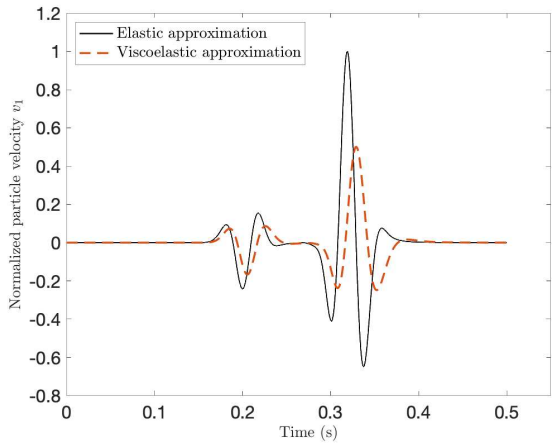

(a) v_1 for elastic and vosocelastic approximation

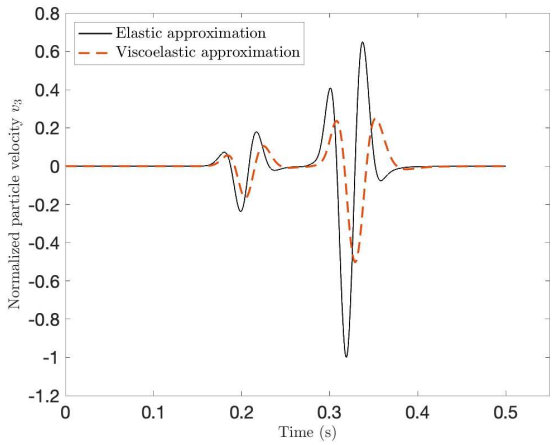

(b) v_3 for elastic and vosocelastic approximation

Figure 5: A comparison of the time history of particle velocities for both elastic and viscoelastic approximations. Subfigures (a) and (b) represent the horizontal and vertical particle velocities, respectively. A difference between elastic and viscoelastic approximation is clearly visible in both by phase and amplitude difference between the traces.

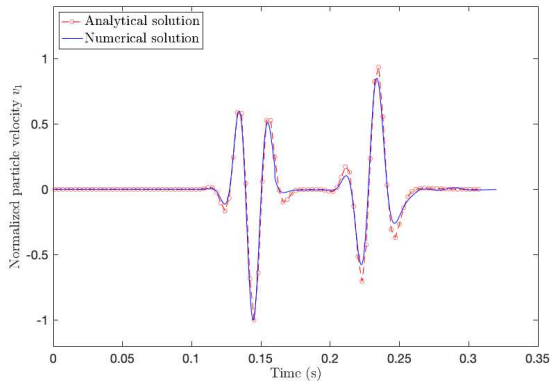

(a) Analytical vs numerical simulation for v_1

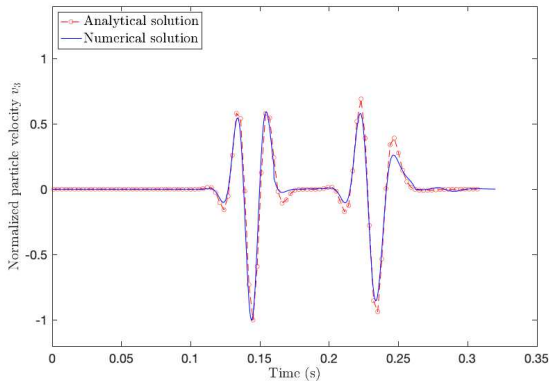

(b) Analytical vs numerical simulation for v_2

Figure 6: A comparison between numerical and analytical solution of viscoelastic wave equation in a homogeneous media. Subfigures (a) and (b) represent the horizontal and vertical particle velocities, respectively. Numerical solution is computed in 2D and for polynomials of degree $N = 3$.

5.3.3. Comparison of elastic and viscoelastic models

To show the effect of the attenuation on wave propagation, we compare numerical solutions of elastic and viscoelastic wave equation in an isotropic sandstone with material properties given in Table 1 (Column 3). Numerical solution are computed in a domain of dimension $[-1\text{ km}, 1\text{ km}] \times [-1\text{ km}, 1\text{ km}]$, and discretized with uniform triangular elements with a minimum edge length of 20.833 m. Figure 5 shows a comparison between the numerical solutions of particle velocities for elastic and viscoelastic equation with $x-$ and $z-$ components represented in Figure 5a and 5b, respectively. The central frequency of the forcing function is $f_0 = 20$ Hz. Polynomials of degree $N = 3$ are used for the simulation. The solution are stored at receiver position $(250\text{ m}, 250\text{ m})$ with source located at $(0\text{ m}, 0\text{ m})$. A difference between the amplitude of elastic and viscoelastic solutions in Figure 5 is due to the attenuation brought in to the system due to the relaxation. The relaxation also results into decreasing the velocity of waves (when compared against the pure elastic

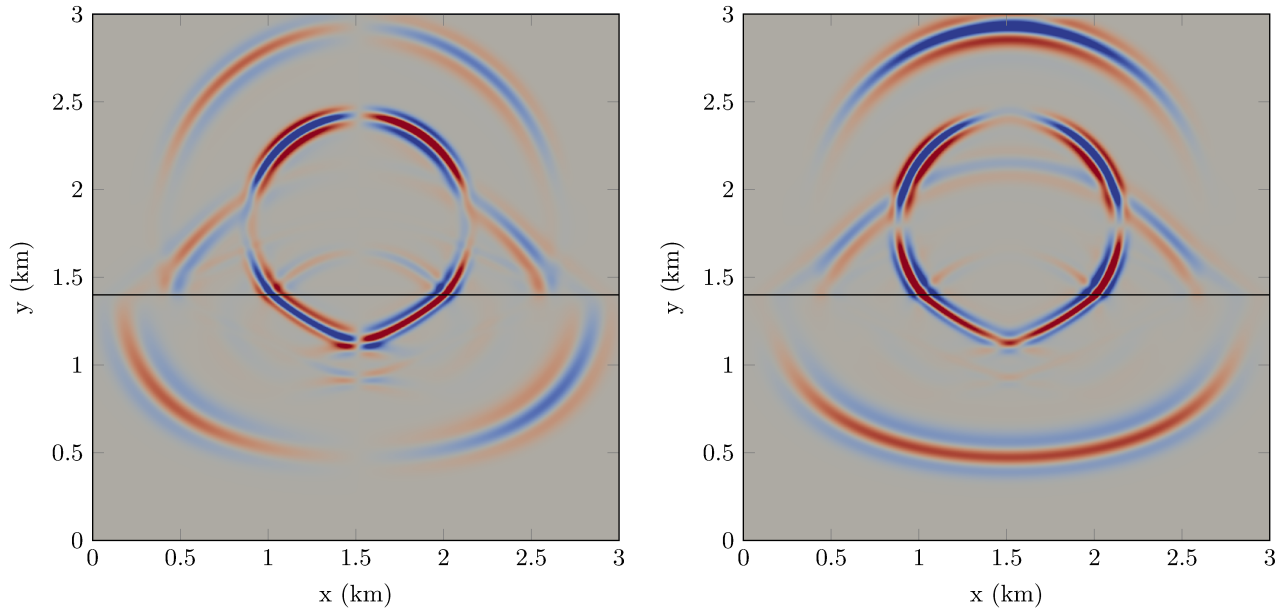

(a) v_1 (b) v_2

Figure 7: Snapshots of particle velocities in the layered model with (a) and (b) showing v_1 and v_2 components at $t = 0.4$ s. The central frequency of the forcing function is 20 Hz. The point source is located at (1.5 km, 1.8 km).The solution is computed using polynomials of degree $N = 3$ and $K = 32,768$.

or loss-less case), which is clearly reflected by the difference in phases between the elastic and viscoelastic solutions, shown in Figure 5.

5.3.4. Comparisons of analytical and numerical solutions

Now, we compare the analytical and numerical solution, computed from our DG method, of 2D viscoelastic wave equation. (25). The analytical solution of isotropic viscoelastic wave equation is computed by Carcione [3] using correspondence principle [4]. The derivation of analytical solution in a homogeneous and isotropic medium is given in Appendix B. The following forcing function is used to compute the analytical solution

$$f(\boldsymbol{x}, t) = \exp\left[-\frac{\Delta\omega^2 (t - t_0)^2}{4}\right] \cos[\bar{\omega}(t - t_0)]\delta(\boldsymbol{x} - \boldsymbol{x}_0), \tag{31}$$

where $\bar{\omega} = 2\pi f_0$ is central angular frequency with $\Delta\omega = \dfrac{\bar{\omega}}{2}$.

To compute the analytical solution one required the frequency spectrum of (31), which is expressed as

$$F(\omega) = \frac{\sqrt{\pi}}{\Delta\omega}\left(\exp\left[-\left(\frac{\omega + \bar{\omega}}{\Delta\omega}\right)\right] + \exp\left[-\left(\frac{\omega - \bar{\omega}}{\Delta\omega}\right)\right]\right)\exp(-\mathrm{i}\omega t_0). \tag{32}$$

Equation (32) also satisfies the condition $F(\bar{\omega} + \Delta\omega) = F(\bar{\omega})/e$, which is the requirement to compute the analytical solution. Figures 6 shows a comparison between time histories of numerical and analytical solutions of viscoelastic wave equation with $x-$ and $z-$ components being represented in Figure 6a and 6b, respectively. Numerical solution are computed in a domain of dimension $[-0.5 \text{ km}, 0.5 \text{ km}] \times [-0.5 \text{ km}, 0.5 \text{ km}]$, which is discretized with uniform triangular elements with a minimum edge length of 4 m. The material properties of isotropic sandstone (Table 1, Column 3) is used to compute the solutions. The central frequency f_0 of forcing function is 45 Hz, which is located at (0 m, 0 m). The forcing function is added to the force corresponding

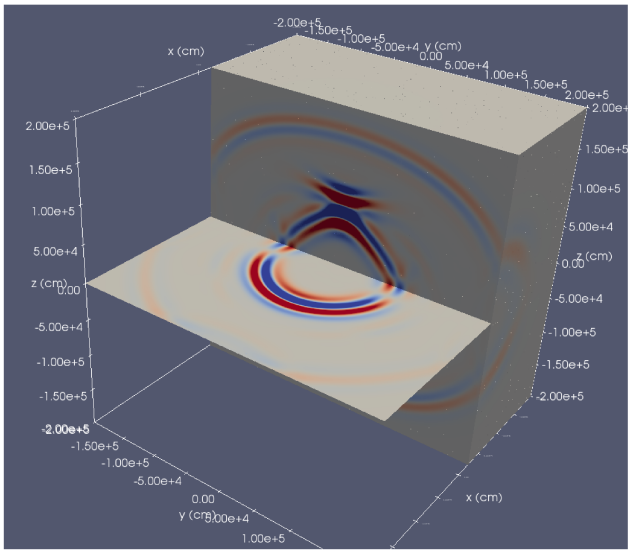

(a) v_1

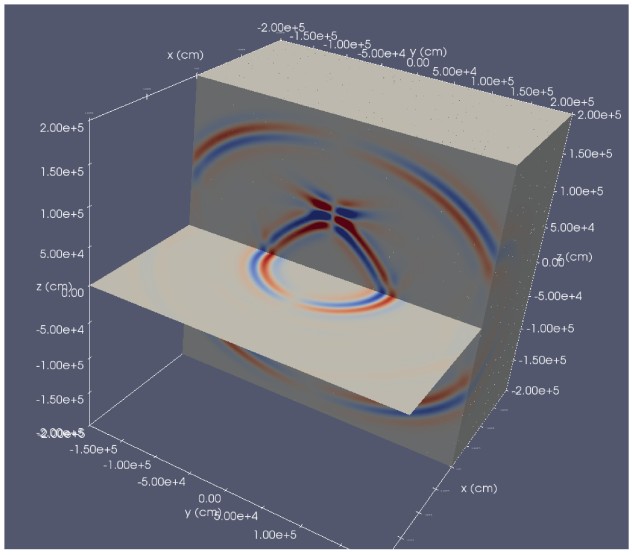

(b) v_2

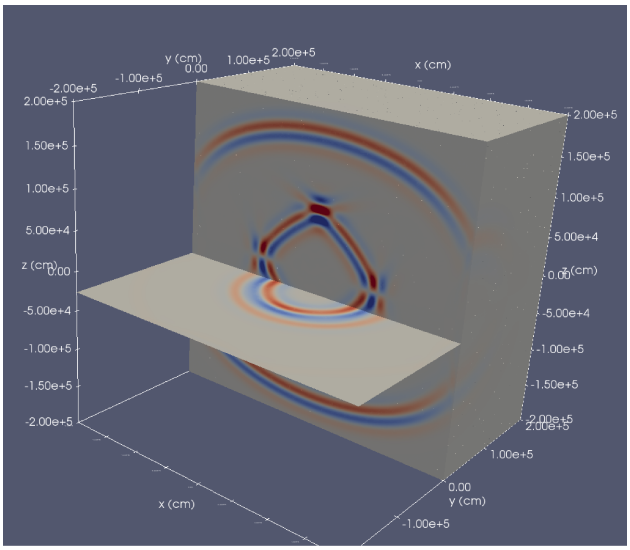

(c) v_3

Figure 8: Snapshots of particle velocities in a 3D homogeneous Orthotropic shale with material properties shown in columns 1 of Table 1. Sub figures (a), (b), and (c) are showing v_1, v_2 and v_3 components at $t = 0.48$ s. The central frequency of the forcing function is 20 Hz. The point source is located at the center of the domain. The solution is computed using polynomials of degree $N = 3$ and $h = 32.5$ m.

to σ_{22}. Polynomials of degree $N = 3$ are used for the simulation. The solution is stored at the node with coordinate $(250\text{ m}, 250\text{ m})$. Figure 6a and 6b show a very good agreement between and analytical and numerical solutions and thus validating the accuracy of the proposed numerical method.

5.3.5. 2D Isotropic-anisotropic layered model

Now, we demonstrate the effect of an interface between two layers of viscoelastic media. In this 2D layered model, the top and bottom layers correspond to isotropic sandstone and orthotropic shale, with material properties given in Column 3 and Column 1 of Table 1, respectively. The domain size is 3 km × 3 km. The

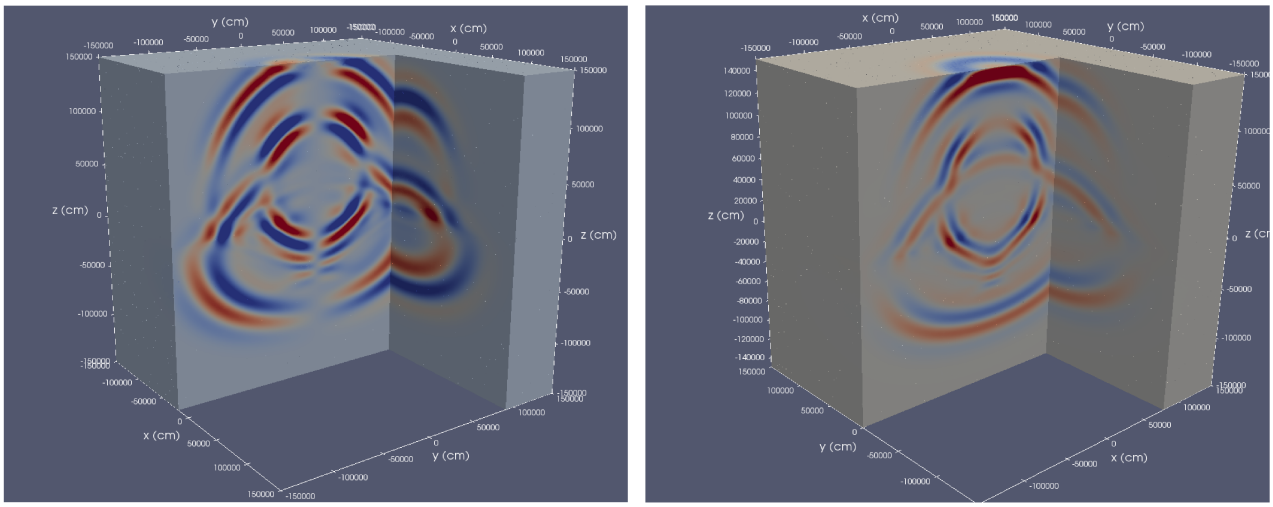

(a) v_2 (b) v_3

Figure 9: Snapshots of particle velocities in a 3D anisotropic heterogeneous two layer model of size 3 km × 3 km × 3 km. Sub figures (a), and (b) are represnt v_2 and v_3 components at $t = 0.4$ s. The central frequency of the forcing function is 20 Hz. The point source is located in the domain at $(0 \text{ km}, 0 \text{ km}, 0.3 \text{ km})$. The solution is computed using polynomials of degree $N = 3$ and $h = 32.5$ m.

minimum edge size of the triangular elements used to discretized the domain is 23.4375 m and polynomials of degree $N = 3$ is used for approximation of numerical solutions. The point source is located at $(1.5 \text{ km}, 1.8 \text{ km})$ with a Ricker wavelet of frequency 20 Hz. The total propagation time is 0.4 s. Snapshots of the x and z components of the particle velocity are shown in Figures 7a and 7b, respectively. The presence of interface results into reflected wavefronts in addition to the direct and transmitted wavefronts and all these three wavefront are clearly shown in Figure 7.

5.3.6. 3D Orthotropic material

Now, we validate our numerical scheme in a homogeneous and anisotropic 3D model. First, we perform a 3D computational experiment for orthotropic shale with the material properties given in Table 1 (Column 1). The size of the computational domain is 4 km × 4 km × 4 km and is discretized by tetrahedral element with a minimum edge length of 32.5 m. The central frequency of the forcing function is $f_0 = 20$ Hz (the frequency for relaxation peak). Polynomials of degree $N = 3$ are used for the simulation. The propagation time is 0.48 μs. Figures 8(a), (b) and (c) represent the $x-$, $y-$ and $z-$ components of the particle velocity of the orthotropic material, respectively. Both modes of waves along with anisotropy can be observed: the P mode and the shear mode (S, inner wavefront). Figure 8 shows that the plane perpendicular to $z-$ direction is a plane of symmetry, as the plane is represented isotropic phenomena.

5.3.7. 3D isotropic-anisotropic layered model

In this example, we illustrate the effect of a two dimensional interface between two layers of the 3D viscoelastic media. The top and bottom layer of 3D model are comprised of isotropic sandstone and orthotropic shale, respectively. The size of the computational domain is 3 km × 3 km × 3 km in the x, y and z directions, respectively. The minimum edge size of the triangular elements used to mesh the domain is 32.5 m. The point source is located at $(0 \text{ km}, 0 \text{ km } 0.4, \text{ km})$ with a Ricker wavelet of frequency 20 Hz. The propagation time is 0.4 s. The simulation is performed using polynomials of degree $N = 3$. Snapshots of the y and z components of the particle velocity are shown in Figures 9a and 9b, respectively. Figure 9 clearly demonstrate the effect the interface responsible for reflected wavefronts of P and shear waves.

5.4. A large 3D heterogeneous subsurface model

We use a 3D reservoir model from Shukla *et al.* [41]. The model is characterized by rock layers, discontinuity, and a surface with undulated topography. The discretized model is shown in Figure 10a. The dimension of the model is (22.8km $\times$ 17.4 km $\times$ 8.0 km) in x, y and z directions, respectively. The domain is discretized with tetrahedral elements with a minimum edge length of 125 m. The top surface of the model is perturbed so that the effects of the topography, assumed as a free surface, could be incorporated into numerical simulations. The central frequency of the forcing function is 20 Hz and polynomials of degree $N = 3$ are used for simulation. Figure 10(b) represent the z- component of the particle velocity at 3.5 s. The various modes of transmissions, reflections and scattering can be clearly seen in Figure 10b.

6. Conclusions

This work presents a high order discontinuous Galerkin method for a new symmetric form of the linear anisotropic viscoelastic wave equations. The method is energy stable and high order accurate for arbitrary stiffness tensors. We confirm the high-order accuracy of the numerical method using an analytic plane wave solution in a viscoelastic media. Finally, we provide computational results for various combinations of homogeneous and heterogeneous medium.

7. Acknowledgments

The authors gratefully thank the sponsors of the Geo-Mathematical Imaging Group at Rice University for providing the resources to carry out this work. Jesse Chan gratefully acknowledges support from the NSF under awards DMS-1719818 and DMS-1712639. MVdH gratefully acknowledges support from the Simons Foundation under the MATH + X program and the NSF under grant DMS-1815143. The authors gratefully acknowledge Dr. José M Carcione of INOGS Italy, for his help in deriving and implementing the analytical solution in a 2D viscoelastic medium.

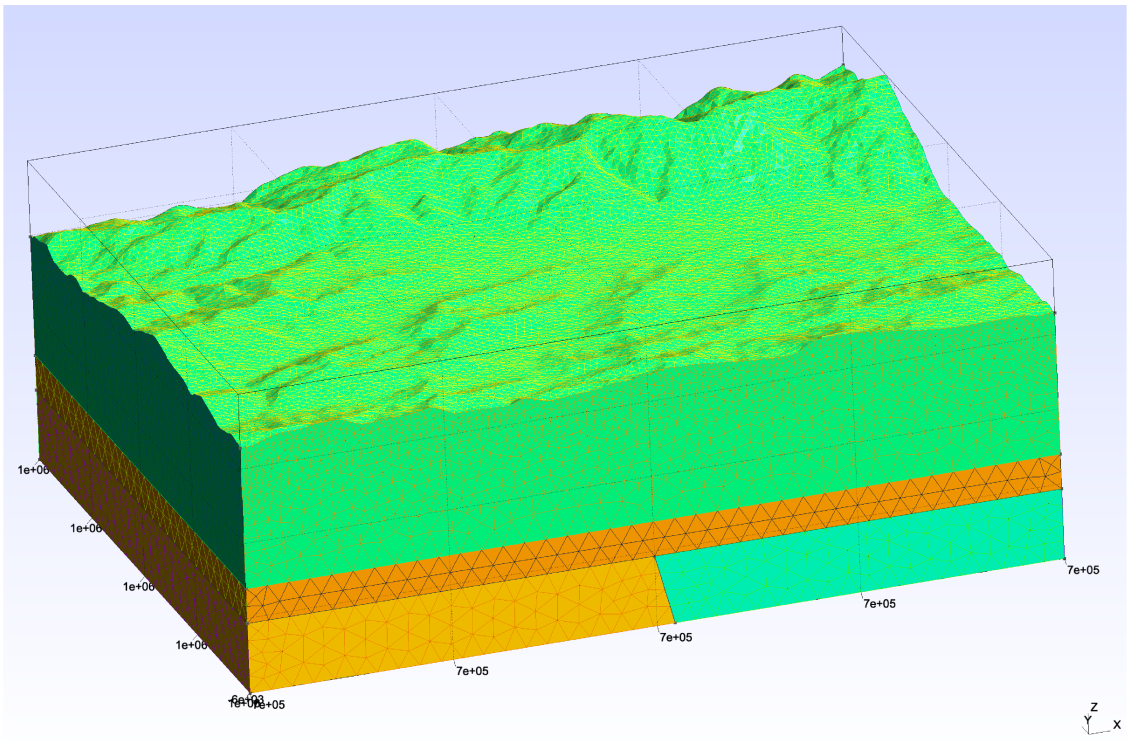

(a) 3D model constructed with topography with minimum edge length of element $h = 125$ m

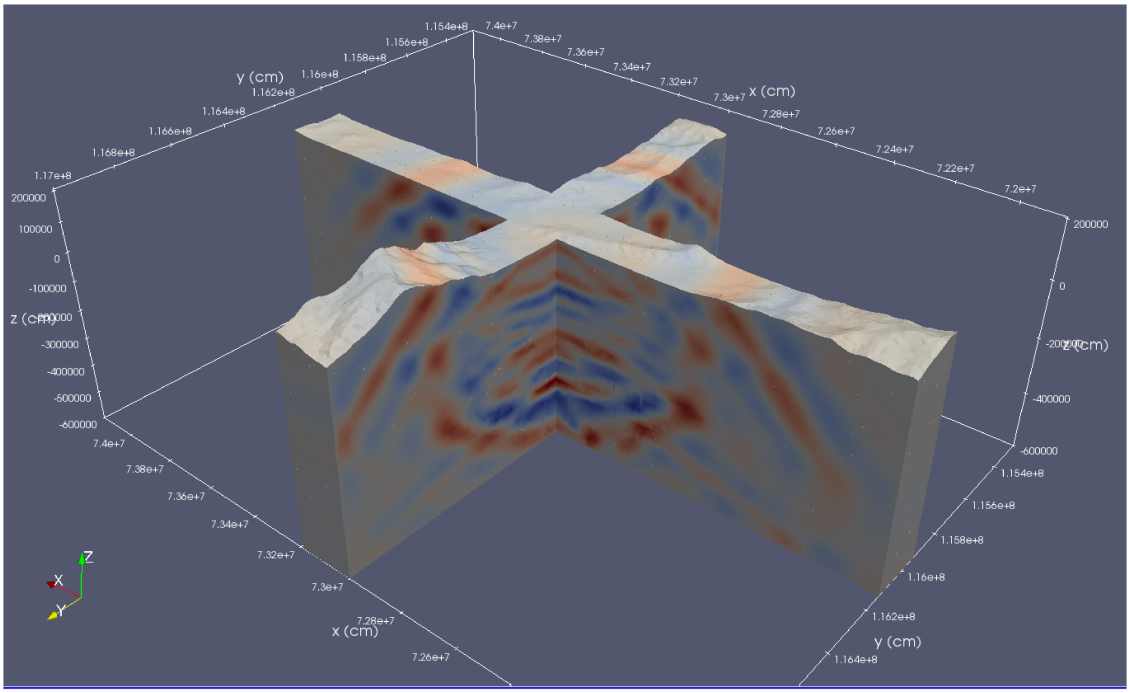

(b) Snapshot of v_3 at $t = 3.5$ s

Figure 10: A 3D snapshot of v_3 for a 3D heterogeneous model constructed with topography on the top surface and a discontinuity in lower most layer. Subfigure (a) shows the 3D model of domain size (22.8 km, 17.4 km 8.0 km) and discretized with tetrahedral element with a minimum edge length of element being $h = 125$ m. Subfigure (b) shows the snapshot of v_3 at 3.5 s. The point source is located in the domain at (11.4 km, -8.7 km, -50 m) . The solution is computed using polynomials of degree $N = 3$.

References

[1] B Hosten, M Deschamps, and Bernhard R Tittmann. Inhomogeneous wave generation and propagation in lossy anisotropic solids. application to the characterization of viscoelastic composite materials. *The Journal of the Acoustical Society of America*, 82(5):1763–1770, 1987.

[2] Rob J Arts and Patrick NJ Rasolofosaon. Approximation of velocity and attenuation in general anisotropic rocks. In *SEG Technical Program Expanded Abstracts 1992*, pages 640–643. Society of Exploration Geophysicists, 1992.

[3] JM Carcione. *Wave Fields in Real Media: Wave Propagation in Anisotropic, Anelastic, Porous and Electromagnetic Media*. Elsevier Science, 2014.

[4] DR Bland. *The Theory of Linear Viscoelasticity, Pergamon Press, Oxford, 1960*.

[5] Morteza M Mehrabadi and Stephen C Cowin. Eigentensors of linear anisotropic elastic materials. *The Quarterly Journal of Mechanics and Applied Mathematics*, 43(1):15–41, 1990.

[6] K Helbig. Foundations of anisotropy for exploration seismics. In *International Journal of Rock Mechanics and Mining Sciences and Geomechanics Abstracts*, volume 1, pages 19A–20A, 1996.

[7] Jose M Carcione. Constitutive model and wave equations for linear, viscoelastic, anisotropic media. *Geophysics*, 60(2):537–548, 1995.

[8] JM Carcione. Wave propagation in anisotropic linear viscoelastic media: Theory and simulated wavefields. *Geophysical Journal International*, 101(3):739–750, 1990.

[9] Peter Moczo, Jozef Kristek, and Martin Gális. *The finite-difference modelling of earthquake motions: Waves and ruptures*. Cambridge University Press, 2014.

[10] Heiner Igel. *Computational Seismology: A Practical Introduction*. Oxford University Press, 2017.

[11] Jean Virieux. P-SV wave propagation in heterogeneous media: Velocity-stress finite-difference method. *Geophysics*, 51(4):889–901, 1986.

[12] Kurt J Marfurt. Accuracy of finite-difference and finite-element modeling of the scalar and elastic wave equations. *Geophysics*, 49(5):533–549, 1984.

[13] Peter Moczo, Johan OA Robertsson, and Leo Eisner. The finite-difference time-domain method for modeling of seismic wave propagation. *Advances in Geophysics*, 48:421–516, 2007.

[14] Thomas Bohlen. Parallel 3-D viscoelastic finite difference seismic modelling. *Computers & Geosciences*, 28(8):887–899, 2002.

[15] Alan R Levander. Fourth-order finite-difference P-SV seismograms. *Geophysics*, 53(11):1425–1436, 1988.

[16] John C Strikwerda. *Finite difference schemes and partial differential equations*, volume 88. Siam, 2004.

[17] Robert Andrew Drainville, Laura Curiel, and Samuel Pichardo. Superposition method for modelling boundaries between media in viscoelastic finite difference time domain simulations. *The Journal of the Acoustical Society of America*, 146(6):4382–4401, 2019.

[18] Ekkehart Tessmer and Dan Kosloff. 3-D elastic modeling with surface topography by a Chebychev spectral method. *Geophysics*, 59(3):464–473, 1994.

[19] José M Carcione. Domain decomposition for wave propagation problems. *Journal of Scientific Computing*, 6(4):453–472, 1991.

[20] Yongtao Yang, Hong Zheng, and MV Sivaselvan. A rigorous and unified mass lumping scheme for higher-order elements. *Computer Methods in Applied Mechanics and Engineering*, 319:491–514, 2017.

[21] E Wendland and HE Schulz. Numerical experiments on mass lumping for the advection-diffusion equation. *Revista Minerva*, 2(2):227–233, 2005.

[22] Hesheng Bao, Jacobo Bielak, Omar Ghattas, Loukas F Kallivokas, David R O'Hallaron, Jonathan R Shewchuk, and Jifeng Xu. Large-scale simulation of elastic wave propagation in heterogeneous media on parallel computers. *Computer Methods in Applied Mechanics and Engineering*, 152(1-2):85–102, 1998.

[23] Anthony T Patera. A spectral element method for fluid dynamics: laminar flow in a channel expansion. *Journal of Computational Physics*, 54(3):468–488, 1984.

[24] G za Seriani and Enrico Priolo. Spectral element method for acoustic wave simulation in heterogeneous media. *Finite Elements in Analysis and Design*, 16(3):337–348, 1994.

[25] Dimitri Komatitsch and Jean-Pierre Vilotte. The spectral element method: An efficient tool to simulate the seismic response of 2D and 3D geological structures. *Bulletin of the Seismological Society of America*, 88(2):368–392, 1998.

[26] Jose M Carcione, Gérard C Herman, and APE Ten Kroode. Seismic Modeling. *Geophysics*, 67(4):1304–1325, 2002.

[27] J.S. Hesthaven and T. Warburton. *Nodal discontinuous Galerkin methods: algorithms, analysis, and applications*, volume 54. Springer, 2007.

[28] A. Klöckner, T. Warburton, J. Bridge, and J.S. Hesthaven. Nodal discontinuous Galerkin methods on graphics processors. *Journal of Computational Physics*, 228(21):7863–7882, 2009.

[29] M. Ainsworth. Dispersive and dissipative behaviour of high order discontinuous Galerkin finite element methods. *Journal of Computational Physics*, 198(1):106–130, 2004.

[30] L.C. Wilcox, G. Stadler, C. Burstedde, and O. Ghattas. A high-order discontinuous Galerkin method for wave propagation through coupled elastic–acoustic media. *Journal of Computational Physics*, 229(24):9373–9396, 2010.

[31] M. Käser, M. Dumbser, J. De La Puente, and H. Igel. An arbitrary high-order discontinuous Galerkin method for elastic waves on unstructured meshes—III. Viscoelastic attenuation. *Geophysical Journal International*, 168(1):224–242, 2007.

[32] J. de la Puente, M. Käser, M. Dumbser, and H. Igel. An arbitrary high-order discontinuous Galerkin method for elastic waves on unstructured meshes—IV. Anisotropy. *Geophysical Journal International*, 169(3):1210–1228, 2007.

[33] R. Ye, M.V. de Hoop, C.L. Petrovitch, L.J. Pyrak-Nolte, and L.C. Wilcox. A discontinuous Galerkin method with a modified penalty flux for the propagation and scattering of acousto-elastic waves. *Geophysical Journal International*, 205(2):1267–1289, 2016.

[34] Timothy Warburton. A low-storage curvilinear discontinuous galerkin method for wave problems. *SIAM Journal on Scientific Computing*, 35(4):A1987–A2012, 2013.

[35] L Lambrecht, A Lamert, W Friederich, T Möller, and MS Boxberg. A nodal discontinuous Galerkin approach to 3-D viscoelastic wave propagation in complex geological media. *Geophysical Journal International*, 212(3):1570–1587, 2018.

[36] Randall J LeVeque et al. *Finite volume methods for hyperbolic problems*, volume 31. Cambridge university press, 2002.

[37] Jesse Chan and T Warburton. On the penalty stabilization mechanism for upwind discontinuous galerkin formulations of first order hyperbolic systems. *Computers & Mathematics with Applications*, 74(12):3099–3110, 2017.

[38] J. Chan. Weight-adjusted discontinuous Galerkin methods: Matrix-valued weights and elastic wave propagation in heterogeneous media. *International Journal for Numerical Methods in Engineering*, 113(12):1779–1809, 2018.

[39] Jesse Chan, Russell J Hewett, and Timothy Warburton. Weight-adjusted discontinuous Galerkin methods: wave propagation in heterogeneous media. *SIAM Journal on Scientific Computing*, 39(6):A2935–A2961, 2017.

[40] Marshall J Leitman and George MC Fisher. The linear theory of viscoelasticity (constitutive equations, creep laws, stress functions, variational principles and differential operators in dynamic and static linear viscoelasticity theory). *Solid-state mechanics 3.(A 73-45495 24-32) Berlin, Springer-Verlag, 1973,*, pages 1–123, 1973.

[41] Khemraj Shukla, Jesse Chan, V Maarten, and Priyank Jaiswal. A weight-adjusted discontinuous Galerkin method for the poroelastic wave equation: penalty fluxes and micro-heterogeneities. *Journal of Computational Physics*, 403:109061, 2020.

[42] Mark H Carpenter and Christopher A Kennedy. Fourth-order 2N-storage Runge-Kutta schemes. 1994.

[43] Eleuterio F Toro. The HLL and HLLC riemann solvers. In *Riemann solvers and numerical methods for fluid dynamics*, pages 315–344. Springer, 2009.

[44] G Eason, J Fulton, and Ian Naismith Sneddon. The generation of waves in an infinite elastic solid by variable body forces. *Philosophical Transactions of the Royal Society of London. Series A, Mathematical and Physical Sciences*, 248(955):575–607, 1956.

Appendix A. Inverse of compliance matrix C

The expressions for r_{ij} in (24) are

$$r_{11} = -\frac{(c_{11}c_{33} - c_{13}^2)}{(c_{11} - c_{12})(c_{11}c_{33} + c_{12}c_{33} - 2c_{13}^2)} \tag{A.1}$$

$$r_{12} = -\frac{(c_{12}c_{33} - c_{13}^2)}{(c_{11} - c_{12})(c_{11}c_{33} + c_{12}c_{33} - 2c_{13}^2)} \tag{A.2}$$

$$r_{13} = -\frac{c_{13}}{(c_{11}c_{33} + c_{12}c_{33} - 2c_{13}^2)} \tag{A.3}$$

$$r_{33} = \frac{(c_{11} + c_{12})}{(c_{11}c_{33} + c_{12}c_{33} - 2c_{13}^2)} \tag{A.4}$$

Appendix B. Analytic solution in a homogeneous viscoelastic media

The solution of the elastic wave equation in an 2-D isotropic medium for an impulsive point force is given by Eason *et al.* [44]. For a force acting in the positive x_3-direction, displacement solutions are expressed as [3]

$$\begin{aligned} u_1(r,t) &= \left(\frac{F_0}{2\pi\rho}\right)\frac{xz}{r^2}\left[G_1(r,t) + G_3(r,t)\right], \\ u_3(r,t) &= \left(\frac{F_0}{2\pi\rho}\right)\frac{1}{r^2}\left[z^2 G_1(r,t) - x^2 G_3(r,t)\right], \end{aligned} \tag{B.1}$$

where F_0 is a the magnitude of the force and $r^2 = x^2 + z^2$, and $G_1(r,t)$ and $G_3(r,t)$ are Green's function expresses as

$$\begin{aligned} G_1(r,t) &= \frac{1}{c_p^2}(t^2 - \tau_p^2)^{-1/2}H(t-\tau_p) + \frac{1}{r^2}(t^2 - \tau_p^2)^{1/2}H(t-\tau_p) - \frac{1}{r^2}(t^2 - \tau_s^2)^{1/2}H(t-\tau_s), \\ G_3(r,t) &= -\frac{1}{c_s^2}(t^2 - \tau_s^2)^{-1/2}H(t-\tau_s) + \frac{1}{r^2}(t^2 - \tau_p^2)^{1/2}H(t-\tau_p) - \frac{1}{r^2}(t^2 - \tau_s^2)^{1/2}H(t-\tau_s), \end{aligned} \tag{B.2}$$

where $\tau_p = \dfrac{r}{c_p}$, $\tau_s = \dfrac{r}{c_s}$ with c_p and c_s being phase velocities of the compressional and shear waves. $H(t)$ is Heaviside function. To recover the anelastic solution the correspondence principle [3] is applied on frequency domain representation of (B.2). We also use following identities of transform pairs of zero- and first-order Hankel function of the second kind

$$\begin{aligned} \int_{-\infty}^{\infty}\frac{1}{\tau^2}\left(t^2 - \tau^2\right)^{1/2}H(t-\tau)\exp(i\omega t)dt &= \frac{\mathrm{i}\pi}{2\omega\tau}H_1^{(2)}(\omega\tau), \\ \int_{-\infty}^{\infty}\frac{1}{\tau^2}\left(t^2 - \tau^2\right)^{-1/2}H(t-\tau)\exp(i\omega t)dt &= -\frac{\mathrm{i}\pi}{2\omega\tau}H_0^{(2)}(\omega\tau). \end{aligned} \tag{B.3}$$

Now, Fourier transform of (B.2) with respect to time yields

$$\widehat{G}_1(r,\omega,c_p,c_s) = -\frac{\mathrm{i}\pi}{2}\left[\frac{1}{(c_p(\omega))^2}H_0^{(2)}\left(\frac{\omega r}{c_p}\right) + \frac{1}{\omega r c_s(\omega)}H_1^{(2)}\left(\frac{\omega r}{c_s(\omega)}\right) - \frac{1}{\omega r c_p(\omega)}H_1^{(2)}\left(\frac{\omega r}{c_p(\omega)}\right)\right], \tag{B.4}$$

$$\widehat{G}_3(r,\omega,c_p,c_s) = \frac{\mathrm{i}\pi}{2}\left[\frac{1}{(c_s(\omega))^2}H_0^{(2)}\left(\frac{\omega r}{c_s(\omega)}\right) - \frac{1}{\omega r c_s(\omega)}H_1^{(2)}\left(\frac{\omega r}{c_s(\omega)}\right) + \frac{1}{\omega r c_p(\omega)}H_1^{(2)}\left(\frac{\omega r}{c_p(\omega)}\right)\right], \tag{B.5}$$

where $c_p(\omega) = \sqrt{\dfrac{(c_{11}+c_{33})M_1(\omega)+c_{33}M_2(\omega)}{\rho}}$, and $c_s(\omega) = \sqrt{\dfrac{c_{33}M_2(\omega)}{\rho}}$ where M_1 and M_2 are recovered from (6), which for isotropic case are as follows,

$$M_{\nu\in\{1,2\}} = \frac{\tau_\sigma^{(\nu)}}{\tau_\epsilon^{(\nu)}}\left(\frac{1+\mathrm{i}\omega\tau_\epsilon^\nu}{1+\mathrm{i}\omega\tau_\sigma^\nu}\right).$$

Now, taking the Fourier transform of (B.1) and using (B.4) and (B.5), we get

$$\begin{aligned} u_1(r,\omega,c_p,c_s) &= \left(\frac{F_0}{2\pi\rho}\right)\frac{xz}{r^2}\left[\widehat{G}_1(r,\omega,c_p,c_s)+\widehat{G}_3(r,\omega,c_p,c_s)\right] \\ u_3(r,\omega,c_p,c_s) &= \left(\frac{F_0}{2\pi\rho}\right)\frac{1}{r^2}\left[z^2\widehat{G}_1(r,\omega,c_p,c_s)-x^2\widehat{G}_3(r,\omega,c_p,c_s)\right] \end{aligned} \tag{B.6}$$

To ensure that solution is real in time, we express (B.6) as

$$u_{1,3}(\omega) = \begin{cases} u_{1,3}(r,\omega,c_p,c_s), & \omega \geqslant 0, \\ u^*_{1,3}(r,-\omega,c_p,c_s), & \omega < 0, \end{cases} \tag{B.7}$$

where asterisk (*) denotes the complex conjugate. Multiplying (B.7) with frequency domain representation of a source time function and then taking the inverse Fourier transform will yield time-domain analytical displacement solution of 2D viscoelastic wave equation (25). The $\widehat{G}_1$ and $\widehat{G}_3$ are considered as zeros due to Hankel's functions being singular.